

FIRST PRINCIPLES STUDY OF THERMOELECTRIC PROPERTIES
OF
ZINC-OXIDE NANOWIRES

THESIS

Presented to the Graduate Council of
Texas State University-San Marcos
in Partial Fulfillment
of the Requirements

for the Degree

Master of SCIENCE

by

Peter D. Heinz, B.S.

San Marcos, Texas
December 2010

FIRST PRINCIPLES STUDY OF THERMOELECTRIC PROPERTIES OF ZINC-
OXIDE NANOWIRES

Committee Members Approved:

Byounghak Lee, Chair

David Donnelly

Gregory F. Spencer

Approved:

J. Michael Willoughby

ACKNOWLEDGEMENTS

Although the present work is presented as my own, it could not have been done without the help of my friends and family. I would like to thank my parents for always providing me with the opportunities to become a better person. Without your support none of this would have been possible. To my son Grayson, thanks for always providing a refreshing break from the monotony of running calculations. And to my wife, thank you for all the understanding and guidance, I love you. I promise that I will make-up for all those weekends I spent in my “cave”.

To my advisor, Dr. Lee, thank you for all the advice and direction you have given me concerning both academics and life. Not only did you make me a better student, but a better person. The lessons I have learned are reflected in every facet of my life, and because of that I owe you a great deal of gratitude. Thank you.

This document was submitted August 9, 2010.

TABLE OF CONTENTS

	Page
ACKNOWLEDGEMENTS	iii
LIST OF FIGURES	vi
ABSTRACT	viii
1: INTRODUCTION	1
1.0 Motivation.....	1
1.1 Thermoelectric Phenomenon	4
1.1.1 Seebeck Effect	4
1.1.2 Peltier Effect	6
1.1.3 Thomsen Effect.....	7
1.1.4 Thermoelectric figure-of-Merit.....	8
1.2 Thermoelectric Properties of Low-Dimensional Materials	11
1.2.1 Thermoelectric Properties of 3-Dimensional Materials.....	12
1.2.2 Thermoelectric Properties of 2-Dimensional Materials.....	13
1.2.3 Thermoelectric Properties of 1-Dimensional Materials.....	15
2: CALCULATION METHODOLOGY	21
2.0 Calculation Overview	21
2.1 Density Functional Theory (DFT)	22
2.2 Boltzmann Transport Theory	27

3: THERMOELECTRIC PROPERTIES OF SILICON	31
3.0 Silicon	31
3.1 Thermoelectric Properties of Bulk silicon	32
3.2 Thermoelectric Properties of Silicon Nanaowires	36
4: THERMOELECTRIC PROPERTIES OF ZINC OXIDE.....	46
4.0 Zinc Oxide	46
4.1 Thermoelectric Properties of Zinc Oxide Bulk.....	47
4.2 Thermoelectric Properties of Zinc Oxide Nanowires	55
5: CONCLUDING REMARKS.....	67

LIST OF FIGURES

Figure	Page
1. Thermoelement.	5
2. Thermocouple - Seebeck Effect.....	6
3. Thermocouple - Peltier Effect.....	7
4. The Conflicting Constituents of The Thermoelectric figure-of-Merit, ZT.....	10
5. Electronic Density-of-States of Low-Dimensional Systems	12
6. 1D Nanowire: Band Gap Dependence on Wire Diameter	16
7. Thermoelectric Properties of Si Nanowires at 300 K.....	20
8. Figure-of-Merit (ZT) of 30 Å Diameter Si Nanowires at 300K.....	20
9. Conventional Unit Cell of Silicon	32
10. Electronic Structure of Si Bulk.....	33
11. Thermoelectric Properties of Si Bulk 8-atom Cell at 300 K.....	36
12. Cross Section of Si Nanowires	38
13. Si NWs Oriented in the [001] Direction	38
14. Electronic Structure of the [001] Si NW	39
15. Electronic Structure of the [011] Si NW	40
16. Electronic Structure of the [111] Si NW	40
17. Thermopower, $S^2\sigma$, of Si NWs at 300 K	43
18. Thermoelectric Properties of Si NWs at 300 K Calculated with BoltzTraP	44
19. Minimum Energy Surface of Bulk ZnO	48

20. Density-of-States of Bulk ZnO	50
21. Band Structure of Bulk ZnO	51
22. Lattice Component of Thermal Conductivity	53
23. Thermoelectric Properties of Bulk ZnO	54
24. ZnO Nanowire Cross-Sections	57
25. ZnO Nanowire Profile	58
26. Electronic Structure of the ZnO NW with 8 Å Diameter	60
27. Electronic Structure of the ZnO NW with 10 Å Diameter	60
28. Electronic Structure of the ZnO NW with 17 Å Diameter	61
29. Thermoelectric Properties of ZnO NWs at 300 K	63
30. Thermopower of ZnO NWs at 300 K	64
31. ZT of ZnO Nanowires.....	65

ABSTRACT

FIRST PRINCIPLES STUDY OF THERMOELECTRIC PROPERTIES OF ZINC-OXIDE NANOWIRES

by

Peter Heinz, B.S.

Texas State University-San Marcos

August 2010

Advisor: Dr. Byounghak Lee.

Nanostructures have a significant promise as potential building blocks for the next generation thermoelectric devices. While the thermal transport properties of bulk materials have been intensely studied, the understanding of nanostructure thermoelectric properties and their interrelation is still incomplete. In this thesis I propose to study the thermoelectric properties of ZnO nanowires as a prototype nanostructure and investigate the relation between the relevant thermoelectric parameters, e.g., electric conductivity, Seebeck coefficient, and thermal conductivity. In addition, I will report on research conducted to determine the dependence of thermoelectric properties on the atomic structure as well as the relationship that nanowire (NW) size bears to these properties. The study will be performed within the density functional theory and Boltzmann transport theory framework.

CHAPTER 1

INTRODUCTION

1.0 Motivation

The energy that drives our modern world comes with a high economic, environmental, and social cost that continues to rise as populations grow and resources diminish. Solutions to the energy crisis must be found to ensure the sustainability of Earth for future generations. The solution on the horizon will probably not be the realization of a sustained fusion reaction or any other single influence, but rather incremental advances in harnessing new and neglected sources of energy. Wind, geothermal, solar, tidal, and other sources of renewable energy are taking center stage as technological advances increase their efficiency and allow for practical applications.

As with the renewable energy sources listed above, thermoelectric devices utilize an existing environmental condition to generate electricity. Instead of pressure gradients causing wind-force to drive a windmill, thermoelectric generators depend on temperature gradients to cause an electromotive-force that propels charge carriers to one end of a material, setting up a potential difference. The reverse is also true. Thermoelectric refrigerators use a power source to drive a current of charge carriers that result in a temperature gradient. Thermoelectric devices may one day offer durable, solid-state replacements for traditional systems based on gears, pumps, and compressors. The problem remains that the efficiency of today's thermoelectric material is inadequate to

compete with conventional power generation and refrigeration. The growing need for alternative power sources is driving a growing interest in developing a new generation of thermoelectric materials. To become competitive with present technologies new thermoelectric materials will need to increase efficiency by a factor of three over present values.¹

Improving the efficiency of thermoelectric devices could make it possible to utilize waste heat from currently neglected sources. The sources of automotive waste heat, e.g. exhaust, brakes, and engines, can be used to increase the efficiency of future hybrid automobiles. Industrial plants, electrical plants, and nuclear power plants, could provide a vital new source of energy by harnessing the heat they produce. Heat from radioactive decay could be utilized for the next generation radioisotope thermoelectric generators, to extend our reach into space. Thermoelectric power generation will also play a role in providing needed energy sources for developing nations in remote areas. A simple wood burning stove or open fire could become a potential cell phone charging station or even provide LED lighting in small villages. Thermoelectric devices have the potential to provide an alternate energy source and be part of the solution to break our dependence on fossil fuel energy. Intensified scientific research in this field will be required to develop the next generation of thermoelectric materials.

Present thermoelectric research is split into two camps; one is searching for new bulk-materials while the other concentrates on low-dimensional systems. New bulk materials of particular interest act like a glass with regards to thermal conductivity (low), while simultaneously acting like a crystal when it comes to electrical conductivity (high). These bulk materials are referred to as phonon-glass electronic-crystals and contain

weakly bound atoms that provide scattering centers for phonons.² The other field of primary focus is the study of low-dimensional thermoelectricity. Reducing dimensions from 3D to 0D (bulk - slab - wire - dot) has shown to introduce quantum confinement effects that alter the electronic structure and enhance the thermoelectric properties over bulk. It is believed that the surfaces introduced by lowering the dimensions play a major role in reducing the thermal conductivity.^{1, 3-6}

The purpose of this study is the investigation of electronic and thermoelectric properties related to 1D low-dimensional systems, nanowires (NWs). The electrical aspects of these low-dimensional systems are explored through density functional theory. The subsequent band structures are then used to determine the thermoelectric properties via the Boltzmann transport theory. Silicon and zinc oxide are explored as potential 1-dimensional thermoelectric materials, because they are cost effective, nontoxic, and easily integrated into present semiconductor manufacturing methods. The effects of different growth directions on the thermoelectric properties are explored in silicon nanowires. The thermoelectric property's dependence on diameter is explored in zinc oxide nanowires.

The rest of Chapter 1 attempts an overview of the thermoelectric phenomenon, density functional theory, and Boltzmann transport theory. Chapter 2 reviews the calculation methodology with a brief look at how the computational codes operate. Chapters 3 and 4 investigate the electronic structure and thermoelectric properties for both bulk and nanowire structures composed of silicon and zinc oxide, respectively. Chapter 5 contains the concluding remarks.

1.1 Thermoelectric Phenomenon

Similar to many other scientific discoveries, the understanding of the thermoelectric effect came through the common curiosity of multiple individuals. These early pioneers sought an understanding of how heat energy and electrical current were interrelated. The first insight into the thermoelectric phenomenon came from Thomas Seebeck, a Baltic German living in the first quarter of the nineteenth century.² Seebeck described the first thermoelectric generator that converted heat energy into voltage. About a decade later, in 1834, a French physicist named Jean Charles Peltier reported thermoelectric refrigeration, essentially the reverse of the Seebeck effect. In the middle of the nineteenth century, Irish-born William Thomson (Lord Kelvin) completed the thermoelectric theory by tying together what Seebeck and Peltier had observed. Lord Kelvin recognized the mathematical relationship between the coefficients defined by Seebeck, Peltier and himself. The subsequent four sections will review these three effects and look at their contribution to the thermoelectric figure-of-merit ZT .

1.1.1 Seebeck Effect

Consider a finite rod of a conducting material that is heated only on one end. The temperature gradient across the rod causes the charge carriers from the heated side to move to the cooler side. In materials other than superconductors below T_C entropy is transported with those charge carriers. They will continue to move to the cooler side of the material until an equilibrium state is established (see Fig. 1). Increasing the temperature gradient from the equilibrium state will cause more charge carriers to move to the cooler side establishing a new potential difference. The maximum voltage is then limited by the melting point of the material.²

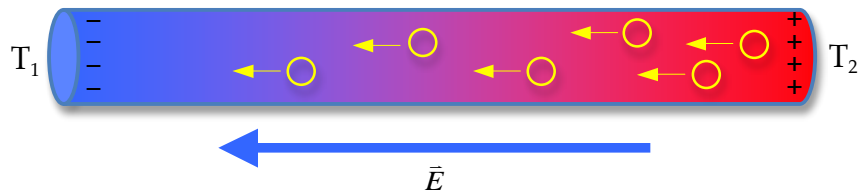


Figure 1. Thermoelement- Charge Carrier Diffusion; where $T_2 > T_1$. In the example above, electrons are the charge carriers represented by the yellow circles. The temp. gradient causes the charge carriers to move toward the cooler side until an equilibrium state is reached. The Seebeck coefficient is the entropy transported with a charge carrier divided by the charge carrier's charge.

If a temperature gradient exists at a junction of two dissimilar conductors connected electrically in series and thermally in parallel, a voltage is produced. This potential drop is the result of the thermoelectric effect first reported by Thomas Seebeck in 1821. Seebeck focused primarily on the power generating properties of a thermocouple known as the Seebeck effect.

$$S = \frac{V}{\Delta T}, \text{ [Eqn: 1]}$$

The voltage generated depends on the Seebeck coefficient S and the temperature difference between the two junctions in the thermocouple, as seen in equation 1.² The Seebeck coefficient is the entropy transported with a charge carrier divided by the carrier's charge.⁷

A functioning thermocouple requires that materials A and B (see Fig. 2) be a p -type/ n -type pair (acceptor/donor). A p -type/ n -type module allows for an exchange between electrons and holes or holes and electrons at the junctions J_1 and J_2 (see Fig. 2), completing the circuit and allowing for either power generation or refrigeration.

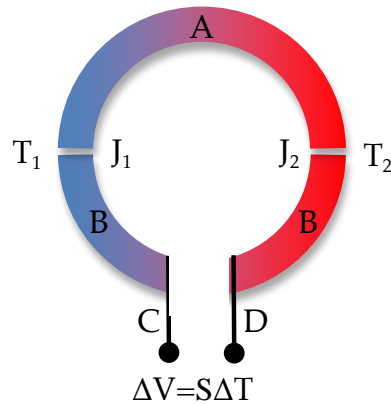


Figure 2. Thermocouple – Seebeck Effect; effect of power generation. A and B are two different conductors. J₁ and J₂ are junctions held at two different temperatures, T₁ and T₂, resulting in the formation of a voltage across points C and D. Materials A and B must be an acceptor/donor pair to complete the electrical circuit. The Seebeck coefficient is represented by S in equation 1.

The sign of the Seebeck coefficient is determined by the direction of current flow. If T_2 is greater than T_1 and the current is flowing clockwise then the Seebeck coefficient is positive, and if the current is counter-clockwise it is negative. The Seebeck coefficient is readily obtained experimentally if the voltage across C and D, and the temperatures of each junction are known.⁸

1.1.2 Peltier Effect

The Peltier effect is the analog to the Seebeck effect. Instead of generating a potential difference across C and D (see Fig. 1) with junctions J₁ and J₂ held at different temperatures, the Peltier effect uses an electromotive source to drive a current, heating one junction and cooling the other.² The effect can be quantitatively described by the Peltier coefficient (see Eqn: 2) and qualitatively described by Figure 3. The Peltier coefficient (π) is determined by the ratio of the current, (I) to the rate of heating (q);

$$\pi = \frac{I}{q}, \text{ [Eqn: 2]}$$

The sign of π is determined by which junction is heated and which is cooled. In Figure 3, if J_1 is cooled and J_2 is heated, then the Peltier coefficient is positive, and negative in the reverse situation when the current flows the opposite direction.

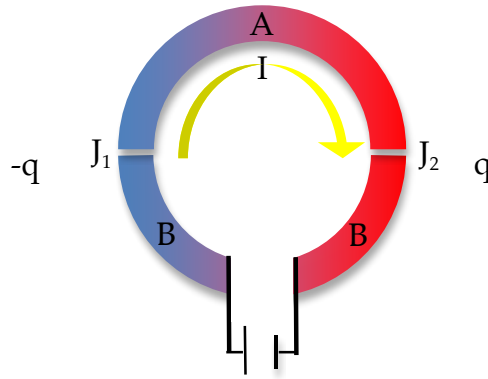


Figure 3. Thermocouple - Peltier Effect; consisting of thermoelectric materials A and B. I is the current from a voltage source flowing clockwise around the circuit and q is the rate of heating. The rate of cooling $-q$ occurs at J_1 while heating q occurs at J_2 . Materials A and B consist of a n -type/ p -type pair where the carriers are predominately electrons in the n -type material and holes in the p -type. Opposite the Seebeck effect, the Peltier effect uses a potential difference to cause a temperature gradient.

1.1.3 Thomson Effect

Looking to connect the thermoelectric effects noticed by Seebeck and Peltier, William Thomson described the third thermoelectric effect. The Thomson effect describes the resulting electric current that develops in a single conductor when a small temperature gradient is applied (see Fig. 2). This relationship is described by the equation;

$$q = \beta I \Delta T, \text{ [Eqn: 3]}$$

where q is the rate of heating, I is electric current, ΔT is change in temperature, and β is the Thomson coefficient. This relationship holds if the temperature difference, ΔT , is small.²

Lord Kelvin, tied all three of the thermoelectric coefficients together in the Kelvin relationships. These equations describe how the Seebeck, Peltier, and the Thomson coefficients interrelate.

$$S_{ab} = \frac{\pi_{ab}}{T}, \text{ [Eqn: 4]}$$

$$\frac{dS_{ab}}{dT} = \frac{\beta_a - \beta_b}{T}, \text{ [Eqn: 5]}$$

Equation 4 relates the Seebeck coefficient to the Peltier coefficient, while Equation 5 relates the Seebeck coefficient with the Thomson coefficient. The Thomson effect and the Kelvin relationships complete the theory encompassed by the thermoelectric phenomena.

1.1.4 Thermoelectric Figure-of-Merit

Although the Seebeck, Peltier, and Thomson coefficients can describe a material's thermoelectric properties, they do not contain the information that enables comparison between two different materials. The thermoelectric coefficients do not include thermal and electrical conductance, which are intrinsic characteristics specific to a particular material. It is known that high thermoelectric efficiency is the result of high electrical conductivity, low thermal conductivity, and a large Seebeck coefficient.³ This relationship is described by the thermoelectric figure-of-merit ZT ;

$$ZT = \left(\frac{S^2 \sigma}{\kappa} \right) T, \text{ [Eqn: 6]}$$

where S is the Seebeck coefficient, σ is the electrical conductivity, κ is the thermal conductivity, and T is temperature. $S^2 \sigma$ is commonly referred to as thermoelectric power.

The thermal conductivity has contributions from the charge carriers moving through the lattice κ_e , and the lattice vibrations κ_l ($\kappa = \kappa_e + \kappa_l$). As carrier concentrations

approach that of metals, the electronic component of thermal conductivity κ_e contributes more to the total thermal conductivity κ . The thermal conductivity of semiconductors is dominated by the lattice vibrations.² For typical thermoelectric materials, 1/3 of the total thermal conductivity is from κ_e .² As will be discussed in Chapter 4, only 10% of the total thermal conductivity of bulk ZnO is contributed by the electronic component of thermal conductivity.^{9, 10} Typically an increase in the electrical conductivity of a bulk material leads to an increase in the thermal conduction as described by the Wiedemann-Franz law;¹¹

$$\kappa = \left(\frac{3k_B^2}{2e^2} \right) \sigma T, \text{ [Eqn: 7]}$$

$$\kappa = L\sigma T, \text{ [Eqn: 8]}$$

where κ ($\kappa = \kappa_e + \kappa_l$) is the total thermal conductivity, k_B is Boltzmann's constant, e is the charge of an electron, σ is electrical conductivity, L is the Lorenz factor, and T is temperature. The Lorenz factor has a numerical value of $2.44 \times 10^{-8} \text{ W}\Omega/\text{K}^2$ calculated from fundamental constants, but experimental values vary slightly between elements. Rubidium and sodium are have Lorenz factors of 2.42×10^{-8} and $2.12 \times 10^{-8} \text{ W}\Omega/\text{K}^2$, respectively.¹²

The Wiedmann-Franz law prohibits the increase of the electrical conductivity independent of thermal conductivity κ for bulk materials. This makes tuning the thermoelectric figure-of-merit a difficult task. Figure 4 illustrates, that for a given material there is a maximum power factor and figure-of-merit optimized for a particular carrier concentration (Figure 4 refers to Bi_2Te_3 in particular). The maximum values of the figure-of-merit usually range from 10^{18} to 10^{21} carriers cm^{-3} . These values are similar

to the concentration of heavily doped semiconductors and makes them primary thermoelectric candidates.²

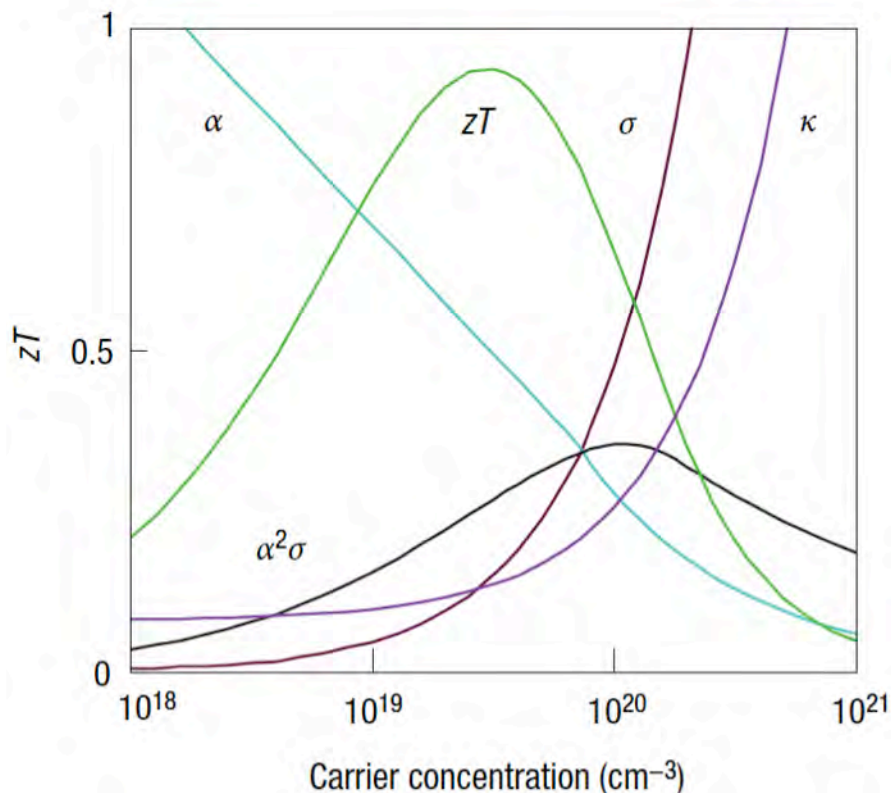


Figure 4. The Conflicting Constituents of the Thermoelectric Figure-of-Merit, ZT . In this figure α is the Seebeck coefficient (blue), σ is the electrical conductivity (maroon), κ is the electrical contribution to the thermal conductivity (purple), $\alpha^2\sigma$ is the power factor (black), and ZT is the thermoelectric figure-of-merit (green). Trends shown from Bi_2Te_3 . Published in Nature (see Ref. 2).

Due to the conflicting nature of the constituents of the figure-of-merit, advancement of thermoelectric devices has been very slow. The best thermoelectric materials commercially available today are alloys of bismuth telluride with a figure-of-merit around one ($ZT \approx 1.0$).³ Thermoelectric (Peltier) coolers with a $ZT \approx 1$ corresponds to 10% Carnot efficiency.¹³ Therefore, 90% of the energy put into the system goes unutilized. Considering that a typical household refrigerator runs at $\sim 45\%$ Carnot efficiency, thermoelectric materials require significant improvement before becoming

viable options. Research working toward the enhancement of ZT is attempting to both 1) discover new bulk materials and 2) tune existing thermoelectric materials with low-dimensional systems. This study neglects phonon-glass/electronic-crystals and other new bulk materials and focuses on low-dimensional systems as a means of increasing ZT. Recent advances on low-dimensional systems, other than nanowires (NWs), will be briefly discussed to provide insight as they apply to this study.

1.2 Thermoelectric Properties of Low-Dimensional Materials

Bulk materials, with the exception of changing the carrier concentration through doping or adjusting the operating temperature, offer little flexibility for thermoelectric tuning. As shown in the previous section the constituents of the thermoelectric figure-of-merit are interrelated for bulk materials. Due to the inflexibility of bulk materials it is difficult to change the electrical conductivity without adversely affecting the thermal conductivity or the Seebeck coefficient. If the physical dimensions of the system are reduced to sizes comparable with the wavelength of an electron (de Broglie $\lambda_{\text{elec.}} \approx 1 \text{ \AA}$), quantum confinement is introduced, altering the electronic structure.^{1, 4-6, 14, 15} The fundamentals of quantum mechanics assert that quantum confinement reduces the number of available energy states resulting in a larger occupancy of the remaining states and a greater difference in energy between states. Theoretically the resulting characteristic sharp peaks in the electronic density-of-states of NW structures suggest a high thermo-power and thus a high ZT.¹⁶ These characteristic sharp peaks can be observed in the zinc oxide NWs discussed in Chapter 4, but not the silicon found in Chapter 3.

The difference in thermoelectric properties of low-dimensional systems compared to bulk materials is the result of different density-of-states for 3D, 2D, 1D, and 0D systems. Figure 5 illustrates the dramatic differences in the density-of-states that can be achieved by moving to low-dimensional systems. Reducing the dimensions of material systems introduces flexibility with regards to tuning the electronic structure for improved thermoelectric efficiency. Low-dimensional systems also increase phonon scattering by introducing interfaces and surfaces.¹ Increased phonon scattering can reduce the lattice component of thermal conductivity, which can significantly improve ZT.

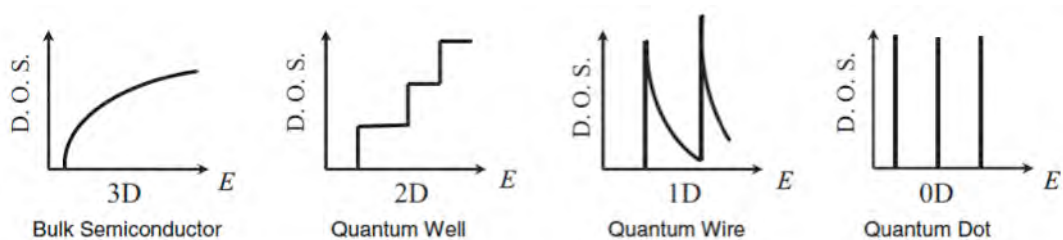


Figure 5. Electronic Density-of-States of Low-Dimensional Systems. a) bulk 3D crystalline semiconductor, b) a 2D quantum well, c) a 1D nanowire or nanotube, and d) a 0D quantum dot. Low dimensionality material systems may also reduce the lattice component of thermal conductivity, enhancing thermoelectric performance. Published in *Advanced Materials*, 2007 (see Ref. 7)

1.2.1 Thermoelectric Properties of 3-D Materials

Thermoelectric effects can be observed in most conducting materials, but those materials may not be considered a true thermoelectric material unless $ZT > 0.5$. The temperature range that optimizes the figure-of-merit categorizes the thermoelectric materials into three groups; low, intermediate, and high. Low-temperature materials operate up to 450 K, intermediate-temperature materials operate from 450-850 K, and high-temperature materials operate up to 1300 K.² This study will focus on low to intermediate temperature thermoelectric materials for clean, durable and sustainable energy generation and refrigeration.

The best low-temperature thermoelectric materials are currently based on bismuth telluride alloys. These alloys have held their standing for the past two decades, and it is doubtful that any appreciable gain in thermoelectric efficiency will be realized from alloys alone.¹ The restriction in gains in efficiency solely through alloys emphasize the need for research in low-dimensional systems. Low-dimensional systems allow for the alteration of the electronic structure through the choice of dimensionality, 3D to 0D. In addition further tuning of ZT can be accomplished through reduced dimensions. The ability to manipulate the thicknesses and distances of layers in a superlattice, the radius and length of a NW, and the three confining dimensions of a quantum dot provides greater control over the electronic structure and therefore over the thermoelectric properties.

1.2.2 Thermoelectric Properties of 2-D Materials

Superlattices or quantum well structures are extensively researched because of the interesting quantum confinement effects they introduce. This section will provide a quick review of a few published articles concerning 2D structures and their effect on the thermoelectric figure-of-merit. Theoretical and experimental literature on lattice mismatched thin films is extensive, but few discuss the thermoelectric effects. Mildred S. Dresselhaus of MIT has authored or co-authored several published works dealing specifically with figure-of-merit of low-dimensional systems.

In 1993 L. D. Hicks and M. S. Dresselhaus published theoretical results exploring the effects of a 2D system on the thermoelectric figure-of-merit. The theoretical investigation proposed that a 2D quantum well structure could increase ZT of bismuth telluride (Bi_2Te_3) based systems over bulk by a factor of fourteen.⁶ Generally speaking,

bulk materials possess only one adjustable parameter, doping. In 2D systems the thickness of both the well and barrier material, as well as the growth direction of the layers affect ZT. Secondly the structure of the superlattice provides a means of reducing thermal conductivity through increased phonon scattering off the lattice mismatched interfaces.^{1, 5, 17} To realize a substantial increase in ZT thermal conductivity will need to be reduced while maintaining a high electrical conductivity.

In 1996 Hicks and Dresselhaus reported the possible enhancement of ZT for a 2D system consisting of PbTe/Pb_{1-x}Eu_xTe superlattices.⁴ The structure studied was composed of thin alternating layers of PbTe and Pb_{1-x}Eu_xTe grown via molecular-beam epitaxy. PbTe is the well material with layer widths ranging from 17 to 55 Å and Pb_{1-x}Eu_xTe is the barrier material with a thickness of 450 Å. This system allows for many variables to tune the electronic structure; the thickness of the layers, the distance between the layers, and even the concentration of Eu in the barrier layer. The experimental results imply a five-fold increase in ZT over bulk values, supporting their previous theoretical claims.

Another set of theoretical 2D calculations carried out recently by Daniel Bilc of MIT, suggests that the increase in ZT is the result of a reduction in thermal conductivity alone. In other words, the increase in ZT is due to the introduction of interfaces created by the lattice mismatches of the bulk materials that make up the superlattice. These interfaces serve to scatter the phonons reducing the thermal conductivity while not adversely affecting the electrical conductivity. Bilc demonstrated through first-principle calculations that the electrical conductivity of a chalcogen (compound containing a group 6 element) superlattice system of (Bi₂Te₃)_m(Sb₂Te₃)_n is not deteriorated from the bulk

values of its constituents while thermal conductivity was significantly reduced.¹⁷

Contradicting the Wiedemann-Franz law derived for bulk materials (see Eqn. 7 & 8) Bilc demonstrated that one could vary thermal conductivity independent of electrical conductivity.

Reducing dimensions from 3D to 2D (bulk to thin film) has been proven to increase ZT by altering the electronic structure and increasing phonon scattering off interfaces. As shown, in Figure 5 reducing the dimensions from 2D to 1D will further enhance the effects of quantum confinement by reducing the number of available states even further, promoting sharp peaks in the density-of-states. 2D systems allow two in-plane directions for phonons to travel freely without potentially scattering off an interface. 1D systems could prove ideal for thermoelectric devices because they offer only one direction for phonons to freely propagate, possibly further reducing the lattice component of thermal conductivity while maintaining a high electrical conductivity.

1.2.3 Thermoelectric Properties of 1-D Materials

1D nanostructures such as NWs are periodic only in the direction parallel to the NW's axis. NW systems offer a few more tuning options over bulk materials; growth direction, radius/diameter, length, and doping. Quantum confinement is introduced when the size of two of the three directions (Cartesian) has been reduced to a length approaching the magnitude of an electron's wavelength. Nanowires of this scale are now possible due to advancements in material engineering. The possibility of validating theories and supporting them with experimental evidence has sparked new interest in the ~200 year old study of thermoelectricity. Figure 6 shows that as a Bi NW's confining

dimensions (radius) are reduced, the band gap increases.¹ The radius of the NW inversely effects both the band gap and ZT.¹⁴

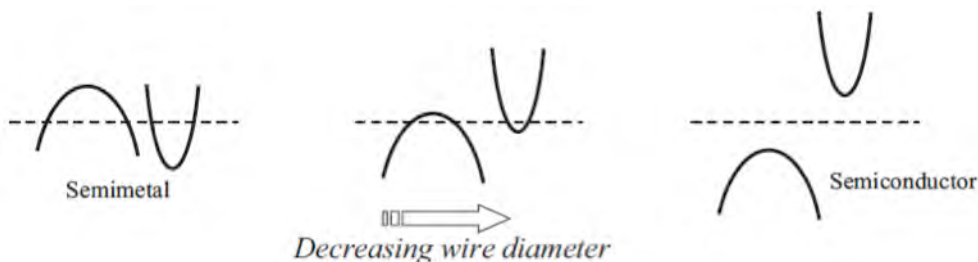


Figure 6. 1D Nanowire: Band Gap Dependence on Wire Diameter. “Schematic diagram of the Bi NW semimetal–semiconductor electronic transition as the lowest conduction sub-band at the L-point moves up in energy, and the highest valence sub-band at the T point [35] (Copyright 1968, American Physical Society) moves down in energy, as the NW diameter dW decreases. a) $dW \gg 50$ nm, b) $dW \sim 50$ nm, c) $dW \ll 50$ nm, the values being appropriate to pure Bi [5]. Copyright 2003, Massachusetts Institute of Technology.”

NWs are often prepared with the use of a dielectric matrix of porous anodic alumina (Al_2O_3). The materials of interest are introduced to the pores of the anodic alumina by pressure injection method,¹⁴ vapor phase method,¹⁸ and electrochemically.¹⁴ A few of the materials used to produce NWs in the ways listed above are Bi,¹⁹ Bi_1 , Sb_x ,²⁰⁻²², and Si^{23} . ZnO NWs can also be grown without the use of the anodic alumina scaffold. Instead, chemical vapor deposition (CVD) can be used to deposit ZnO onto a gold substrate that acts as a catalyst for NW growth.²⁴

Silicon has been, and still remains the backbone of the semiconductor industry because it is inexpensive, non-toxic, and easily integrated into present semiconductor manufacturing methods. A material is considered thermoelectric if ZT is greater than ~ 0.5 . With a ZT of ~ 0.01 bulk silicon would not be classified as a thermoelectric material, but if efficiency were to increase by an order of magnitude it could provide a cost effective thermoelectric module for capturing industrial waste heat as one example. The low ZT can be partially attributed to the high thermal conductivity of bulk silicon

(~ 100 W/Km).^{25,26} Low-dimensional systems can increase scattering off surfaces and interfaces which could potentially reduce thermal conductivity providing a means of increasing ZT. Both silicon NWs and their antithesis, porous silicon, have been studied for their thermoelectric properties.^{25, 27} In both cases a marked increase in the thermoelectric figure-of-merit over bulk silicon was reported. The results of the two silicon articles, discussed below, will be used as a benchmark for the calculation methodology employed on the ZnO NWs discussed in Chapter 4.

Gullia Galli *et al.* performed density functional theory calculations in conjunction with the Boltzmann transport theory to determine the thermoelectric properties of silicon NWs of different axis orientations and diameters ranging from 10 to 30 Å. It was shown that a Si NW grown in the [001] direction, with a diameter of 11 Å, had a ZT of ~ 2.5 .²⁷ This represents an increase of two orders of magnitude over bulk silicon ($ZT_{\text{Si bulk}} \sim 0.01$). Similar calculations were carried out for nanoporous silicon, but the increase of ZT reported was only by one order of magnitude.²⁵

Recent experimental reports have demonstrated the synthesis of silicon NWs with control over size, growth direction, and surface structure has been achieved.^{23, 28-30} The feasibility of Si NWs is encouraging new research into the effect of varying the growth direction, wire diameter, and surface structure on the electrical, optical, and thermoelectric properties of hydrogen-passivated silicon NWs. The calculation methodology employed by Galli *et al.* can be broken into two main steps. Density functional theory was used to determine the ground state electronic structure $E_0(n, \mathbf{k})$ for each of the silicon NWs. The electronic structure $E_0(n, \mathbf{k})$ was then used within the framework of Boltzmann transport theory to determine the thermoelectric properties of

each wire. The results of the Galli *et al.* study were published in two separate papers; one focused primarily on the electronic properties (2006), and the other on the thermoelectric properties (2008).^{27, 31}

The first paper, published in 2006, determined the electronic structure of silicon NWs with diameters ranging from 10 to 30 Å for three different growth directions; the [001], [011], and the [111]. Three different surface structures were considered in the paper, but it was determined that a surface terminated in canted SiH₂ was energetically favorable over a symmetric SiH₂ and a (2x1) surface reconstruction.³¹ All the electronic structures and subsequent thermoelectric properties reported by Galli *et al.* utilized the canted silicon dihydride surface termination. A clean Si surface, exposed to vacuum, will have broken bonds that introduce surface states. To avoid in-gap states in electronic structure calculations the dangling bonds are often terminated with an atom or molecule. Each silicon atom has four bonds to neighboring atoms in a diamond structure. Silicon also has four valence electrons, therefore each atom provides one electron per bond. The simplest method terminates each dangling bond with a single hydrogen atom, maintaining bulk bond angle but half the bond length. Unlike the canted SiH₂ used by Galli *et al.*, the silicon NWs calculations reported in Chapter 3 utilize a single-hydrogen termination scheme.

It is reported that as the diameter of the wire increased from 10 to 30 Å, the gap decreased from 2.35 to 0.88 eV for the [001] NWs, from 1.72 to 0.72 eV for [011] NWs, and from 2.12 to 0.85 for the [111] NWs. As a reference, the calculated band gap reported by Galli *et al.* for bulk silicon was 0.54 eV,³¹ about half of the experimental value of 1.11 eV. These values are comparable with other theoretical calculations of Si

NWs.^{32, 33} As expected the band gap is inversely proportional to the diameter of the wire, reflecting the effects of quantum confinement.

In 2008 the thermoelectric properties of hydrogen-passivated (canted SiH₂) silicon NWs were calculated using Boltzmann transport theory within the constant-relaxation-time approximation. Through the Boltzmann transport equation (BTE) the electrical conductivity σ , electronic component of thermal conductivity κ_e , and the Seebeck coefficient S are calculated from the ground state electronic structure determined using density functional theory. The value for the relaxation time τ was determined by fitting the calculated mobility to experimental carrier concentration dependent mobility data for bulk Si. In addition to the relaxation time τ , the other unknown input parameter is the lattice component of thermal conductivity, κ_l . Boltzmann transport theory does not give any information about the lattice component of thermal conductivity κ_l , which is often the dominant contributor to total thermal conductivity, as high as 90% in the case of ZnO.^{9, 10} Through molecular dynamic (MD) calculations Galli *et al.* determined the lattice component of thermal conductivity to be ~ 2 W/Km for the ~ 10 Å diameter Si NW, in agreement with other reported values.^{34, 35} The lattice component of thermal conductivity was assumed to be independent of the growth direction. Therefore 2 W/Km was used for the [001], [011], and the [111] growth directions.

Figures 7 & 8 indicate that the *n*-type [001] NW (blue-solid line) has the highest value for the figure-of-merit $ZT \sim 2.5$, optimized at a carrier concentration of $\sim 10^{20}$ cm⁻³. Galli *et al.* did not report any values for bulk silicon, but using a similar methodology, Grossman *et al.* calculated ZT for bulk silicon and found a value of ~ 0.003 .²⁵ Figure 8

shows the effects of changing the lattice thermal conductivity by one order of magnitude on ZT.

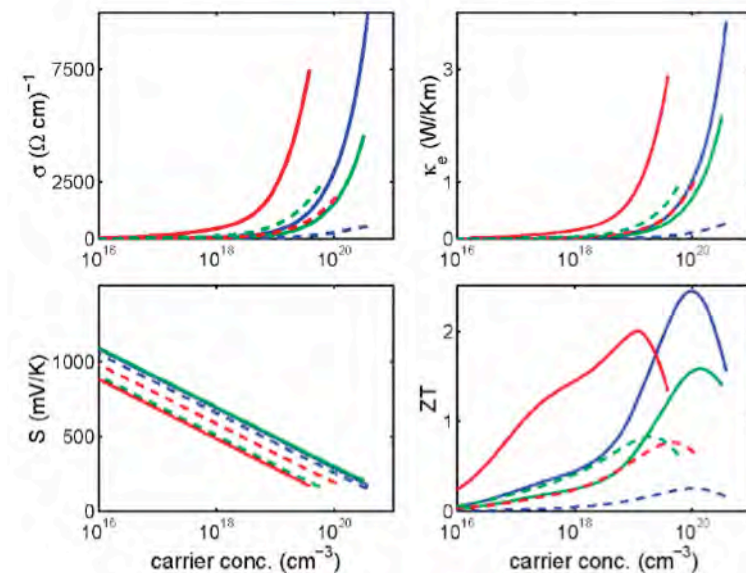


Figure 7. Thermoelectric Properties of Si Nanowires at 300 K; electrical conductivity (σ), electronic thermal conductivity (κ_e), Seebeck coefficient (S), and the thermoelectric figure-of-merit (ZT) of p-type (dashed lines) and n-type (solid lines) doped 11 Å Si NWs grown along the [001] (blue), [011] (red), and [111] (green) directions. For ZT $\kappa_l = 2$ W/Km was used. Published in Nano Letters (see Ref. 1).

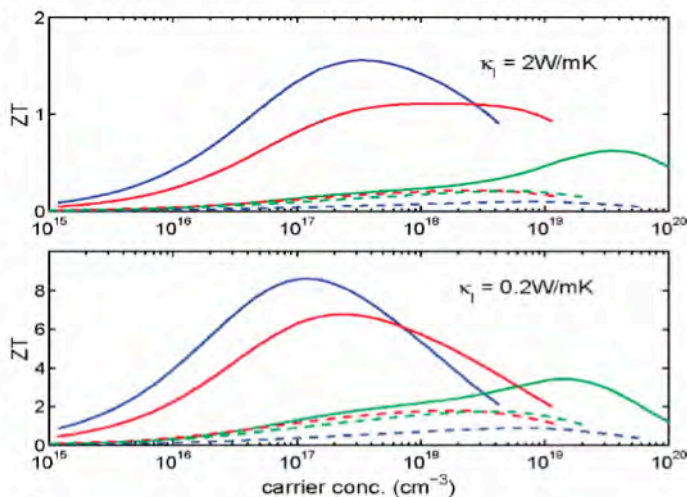


Figure 8. Figure-of-Merit (ZT) of 30 Å Diameter Si Nanowires at 300K. The upper panel was computed assuming $\kappa_l = 2$ W/Km and the lower panel was computed assuming $\kappa_l = 0.2$ W/Km. The smaller κ_l was arbitrarily chosen because it would result in a $ZT \sim 1.0$ for the 30 Å diameter wire. Colors represent; p-type (dashed lines) and n-type (solid lines) doped 30 Å Si NWs grown along the [001] (blue), [011] (red), and [111] (green) directions.

CHAPTER 2

CALCULATION METHODOLOGY

2.0 Calculation Overview

The intention of this study is to calculate the thermoelectric properties of zinc oxide NWs, but first a consistent method must be established and benchmarked against the results of others. Once confidence in the employed methodology is established, it will be used to explore the unknown thermoelectric properties of ZnO NWs. The calculations and subsequent discussions found in Chapter 3 will compare the thermoelectric properties of bulk silicon against what was reported by Grossman *et al.* in 2008.²⁵ The results calculated for silicon NWs will be benchmarked against the result reported by Galli *et al.* of the same year.²⁷

The methodology for this study is split into two major steps; 1) a density functional theory calculation, and 2) the application of the Boltzmann transport theory. Density functional theory, as implemented in VASP³⁶⁻³⁸, is used to find both the minimum energy structure and the ground-state electronic structure in the form of $E_0(n,\mathbf{k})$. The term $E_0(n,\mathbf{k})$ represents the electron energy of band n with wave vector \mathbf{k} . Boltzmann transport theory utilizes the $E_0(n,\mathbf{k})$ data from a density functional theory calculation to determine the thermoelectric properties. The Boltzmann transport code, BoltzTraP, is used for all thermoelectric calculations.³⁹

2.1 Density Functional Theory (DFT)

The fundamentals of quantum mechanics state that the wavefunction (Ψ) contains all the information about a system including, energy, momentum, position, and particle density.⁴⁰ The textbook method of calculating Ψ is to specify a potential $v(\mathbf{r})$, insert $v(\mathbf{r})$ into the Schrödinger equation and solve for Ψ . This is the same for a single-body system or a many-body system; the only difference is in the choice of $v(\mathbf{r})$ and the complexity it can introduce. The Schrödinger equation (SE) for a single-body system is illustrated below;

$$\left[-\frac{\hbar^2 \nabla^2}{2m} + v(\mathbf{r}) \right] \Psi(\mathbf{r}) = \varepsilon \Psi(\mathbf{r}), \text{ [Eqn: 9]}$$

where \hbar is Planck's constant, m is the mass of the particle, $v(\mathbf{r})$ is the potential that characterizes the system, Ψ is the wave function, and ε is the energy.⁴¹ For a many-body Coulomb system the Schrödinger equation becomes;

$$\left[\sum_i^N \left(-\frac{\hbar^2 \nabla^2}{2m} + v(\mathbf{r}_i) \right) + \sum U(\mathbf{r}_i, \mathbf{r}_j) \right] \Psi(\mathbf{r}_1, \mathbf{r}_2, \dots, \mathbf{r}_N) = E \Psi(\mathbf{r}_1, \mathbf{r}_2, \dots, \mathbf{r}_N), \text{ [Eqn: 10]}$$

here N is the number of electrons and $U(\mathbf{r}_i, \mathbf{r}_j)$ is the electron-electron interaction. All observables are attainable by taking the expectation value of an operator using the Ψ determined with the SE.⁴⁰

The additional electron-electron interactions of the many-body SE make solving it complex and computationally expensive. Solving the Schrödinger equation for a full many-body wave function, for systems with more than a few hundred electrons is still beyond modern computational power.⁴¹ An alternative method is to apply the density functional theory to turn the many-body problem into a single-body problem by eliminating all the electron-electron interactions. The framework that makes this possible

is based on the Hohenberg-Kohn (HK) theorem⁴² and the Kohn-Sham (KS) scheme⁴³.

Some aspects of the two contributions will be briefly reviewed below.

The HK theorem states that the non-degenerate ground-state energy is a functional of the ground-state charge density ($n_0(\mathbf{r})$). Because the Ψ contains all the information about a system, any ground-state operator is then a functional of the ground-state density;⁴²

$$O_0[n_0] = \langle \Psi_0[n_0] | \hat{O}_0 | \Psi_0[n_0] \rangle, \quad [Eqn: 11]$$

Where O_0 is a general observable and \hat{O}_0 is an operator used to obtain O_0 . Equation 11 is referred to as the 1st HK theorem. A more specific observable is the ground-state energy for a system of potential v ;

$$E_{v,0} = E_v[n_0] = \langle \Psi_0[n_0] | \hat{H} | \Psi_0[n_0] \rangle, \quad [Eqn: 12]$$

Equation 12 demonstrates that to find the ground-state energy E_0 , the expectation value of Hamiltonian is taken with respect to the ground-state wavefunction (Ψ_0).

Not only must the Ψ_0 reproduce the ground-state density, it must minimize the energy. This statement is summed up in the following equations;

$$E_{v,0} = \min_{\Psi \rightarrow n_0} \langle \Psi_0[n_0] | \hat{H} | \Psi_0[n_0] \rangle, \quad [Eqn: 13]$$

The operator for energy is the Hamiltonian \hat{H} , $\hat{H} = \hat{T} + \hat{U} + \hat{V}$.

$$E_{v,0} = \min_{\Psi \rightarrow n_0} \langle \Psi_0[n_0] | \hat{T} + \hat{U} + \hat{V} | \Psi_0[n_0] \rangle, \quad [Eqn: 14]$$

The kinetic energy T and the electron-electron interaction U are independent of the potential V . As a result, only the potential V needs to be defined with respect to the particle density. Equation 13 and 14 can then be reduced;

$$E_{v,0} = \min_{\Psi \rightarrow n_0} \langle \Psi_0[n_0] | \hat{T} + \hat{U} | \Psi_0[n_0] \rangle + \int d^3r n(\mathbf{r}) v(\mathbf{r}), \quad [Eqn: 15]$$

By the variational principle the right side of equation 15 has two parts, distinguishing the independence of the potential energy from the kinetic energy and electron-electron interactions.

Another aspect of the HK theorem states that calculating the expectation values of the Hamiltonian with respect to a Ψ other than the Ψ_0 will always give values larger than the ground state energy. This implies that if the energy is calculated with a trial density n' , where $n_0 \neq n'$, a value lower than the ground state energy E_0 is not accessible. This concept is expressed in equation 16 and is referred to as the 2nd HK theorem.

$$E_v[n_0] \leq E_v[n'], \text{ [Eqn: 16]}$$

The HK theorem provides a way to by-pass the many-body Schrödinger equation because it is assumed that the Ψ and therefore the observables are all functionals of particle density, i.e. $O_0 = O[n_0]$. Even with this simplification there is still the problem of electron-electron interactions (U). Walter Kohn and Lu Jeu Sham introduced a concept to further simplify the calculation of desired observables by mapping the original interacting system onto a non-interacting system while preserving the electron density n . This allows for a systematic map of the many-body problem with U onto a single-body problem without U .⁴³ The energy functional for the non-interacting system looks like;

$$E_s[n] = \langle \Psi | \hat{T}_s + \hat{V}_s | \Psi \rangle, \text{ [Eqn: 17]}$$

where;

$$\hat{T}_s + \hat{V}_s = \hat{T} + \hat{U} + \hat{V}, \text{ [Eqn: 18]}$$

T_s is the kinetic energy of an non-interacting system and V_s is the external effective potential, often called the Kohn-Sham potential. The external effective potential of a fictitious single-body system is the sum of the many-body potential plus the Hartree

potential and the exchange-correlation potentials;

$$v_S = v + v_H + v_{XC}, \text{ [Eqn: 19]}$$

Where the Hartree potential v_H describes the electron-electron Coulomb repulsion and exchange-correlation potentials v_{XC} describes the variation of the exchange-correlation energy E_{XC} with respect to the charge density. Therefore the Schrödinger equation (see Equation 9 & 10) for the auxiliary single-body system becomes;

$$\left[-\frac{\hbar^2 \nabla^2}{2m} + v_S(\vec{r}) \right] \Phi(\vec{r}) = \epsilon \Phi(\vec{r}), \text{ [Eqn: 20]}$$

here the Kohn-Sham wavefunction ($\Phi(\mathbf{r})$) which represents the electronic states of the fictitious non-interacting system. It should be noted that the $\Phi(\mathbf{r})$ bears no physical meaning. The Hohenberg-Kohn theorem bypasses the SE through a minimization of the functional $E[n]$, while the Kohn-Sham solves a modified, non-interacting Schrödinger equation. The assumption that the charge density of the non-interacting system, calculated with the auxiliary equation reproduces the charge density of the interacting system, makes DFT possible;

$$n(\vec{r}) \equiv n_S(\vec{r}) = \sum_i^N f_i |\Phi_i|^2, \text{ [Eqn: 21]}$$

here f_i is the occupation of the i^{th} orbital. These assumptions allow DFT to be a powerful tool for calculating binding energies in chemistry or electronic structure in physics. In 1998 Walter Kohn was awarded the Nobel Prize in Chemistry for his contributions to the fields of computational chemistry.

In this report density functional theory is used to determine the ground-state ionic structure, band structure, and the electronic density-of-states. The first step in the electronic structure calculations is to determine the minimum energy crystal structure.

The importance of obtaining the minimum energy structure can be realized through the HK theorem; the structure that minimizes energy $E_{v,0}$ corresponds to the structure that yields the ground-state charge density n_0 . The n_0 of the minimum energy structure is used to calculate the ground state electronic structure. Once the minimum energy lattice parameters are known a converged self-consistent charge density can be used to calculate the electronic structure. The band structure gives you the energy as a function of band number n and wave vector \mathbf{k} , $E(n, \mathbf{k})$. Excitation energies, effective mass, and group velocity are a few properties that can be parsed from the band structure data. For this report the band structure will be used to analyze the dispersion and difference between (band gap) the highest valence bands and lowest conduction bands. The calculated density-of-states (DOS) reveals the number of charge carriers, in a given volume, for the infinitesimal energy range of $E+\partial E$. Good thermoelectric materials usually have characteristic “sharp peaks” in the DOS around the edges of the band gap as suggested by M. S. Dresselhaus.¹

The implementation of the HK theorem and KS equations can be found in many density functional codes. Two of the most popular are the Vienna Ab-initio Simulation Package, VASP³⁶⁻³⁸ (pseudopotential scheme), and WIEN2K⁴³ (full-electron scheme). In this study VASP will be used for all electronic structures calculations. VASP is a flexible code for “ab-initio quantum-mechanical molecular dynamics simulations” with a plane wave basis set that utilizes pseudopotentials and has the ability to incorporate the projector-augmented method (PAW).³⁷ Unless stated otherwise all calculations reported in this study utilized the PAW method with the generalized-gradient approximation of Perdew, Burke, and Ernzerhof (PBE).⁴⁴

2.2 Boltzmann Transport Theory

Boltzmann transport theory provides a method of calculating the thermoelectric transport coefficients with little computational effort. The theory describes the evolution of a distribution function $f(n, \mathbf{k})$, influenced by an external electric field \mathbf{E} and a temperature gradient ∇T . This distribution function $f(n, \mathbf{k})$ provides the probability of finding an electron in band n with wave vector \mathbf{k} . The Boltzmann equation is;

$$-\left(\frac{\partial f^0(n, \vec{k})}{\partial \varepsilon(n, \vec{k})}\right) \vec{v}(n, \vec{k}) \left[\frac{\varepsilon(n, \vec{k})}{T} \nabla T + e \vec{E} - \nabla \mu \right] = -\left(\frac{\partial g(n, \vec{k})}{\partial t}\right)_{sc}, \quad [Eqn: 22]$$

Where $f^0(n, \mathbf{k})$ is the equilibrium distribution function, $\varepsilon(n, \mathbf{k})$ is the energy of an electron in band n with wave vector \mathbf{k} , $\mathbf{v}(n, \mathbf{k})$ is the velocity of an electron in band n with wave vector \mathbf{k} , T is the temperature, e is the charge of an electron, \mathbf{E} is the external electric field, and μ is the chemical potential.⁴⁵ The term $g(n, \mathbf{k})$ is the difference between the equilibrium Fermi function $f^0(n, \mathbf{k})$ and the Fermi function influenced by an external electric field or temperature gradient $f(n, \mathbf{k})$. To simplify the Boltzmann equation further the constant relaxation time approximation (RTA) is adopted. In this approximation the relaxation time is assumed to be independent of position and velocity. The relaxation time τ represents the time it takes for an electron distribution to relax to the equilibrium Fermi distribution from a non-equilibrium state. Within RTA the Boltzmann transport equation becomes;

$$-\left(\frac{\partial f^0(n, \vec{k})}{\partial \varepsilon(n, \vec{k})}\right) \vec{v}(n, \vec{k}) \left[\frac{\varepsilon(n, \vec{k})}{T} \nabla T + e \vec{E} - \nabla \mu \right] = -\frac{g(n, \vec{k})}{\tau}, \quad [Eqn: 23]$$

Here the right side has been replaced with the RTA. Because $g(n, \mathbf{k}) = f(n, \mathbf{k}) - f^0(n, \mathbf{k})$ it is now possible to solve for $f(n, \mathbf{k})$.⁴⁵ All that is needed is band structure data $\varepsilon(n, \mathbf{k})$ from

which terms in the Boltzmann equation may be calculated, group velocity $\mathbf{v}(n, \mathbf{k})$ as an example;

$$\bar{v}(n, \bar{k}) = \frac{1}{\hbar} \left(\frac{\partial \mathcal{E}(n, \bar{k})}{\partial \bar{k}} \right), \text{ [Eqn: 24]}$$

Now that the non-equilibrium distribution function $f(n, \mathbf{k})$ is known, the thermoelectric properties can be calculated through electrical-current density and heat-current density known as the Onsager relations (see Equation 27 & 28).

$$J = -\frac{16\pi e\sqrt{2m}}{3h^3} \int E^{3/2} \tau(E) \frac{\partial f_0}{\partial E} \left(\frac{E-\mu}{T} \nabla T + \nabla \mu + eE_0 \right) dE, \text{ [Eqn: 25]}$$

$$J_Q = -\frac{16\pi\sqrt{2m}}{3h^3} \int E^{3/2} (E-\mu) \tau(E) \frac{\partial f_0}{\partial E} \left(\frac{E-\mu}{T} \nabla T + \nabla \mu + eE_0 \right) dE, \text{ [Eqn: 26]}$$

The evaluation of the two equations above result in the Onsager relations seen below¹²;

$$\vec{j} = \sigma E_0 - \sigma S \nabla T, \text{ [Eqn: 27]}$$

$$\vec{j} = \sigma S T E_0 - \kappa' \nabla T, \text{ [Eqn: 28]}$$

Where σ is the electric conductivity, S is the Seebeck coefficient, E_0 is an external electric field, and ∇T is a temperature gradient. The term κ' is related to the thermal conductivity and derived from electrical conductivity through the Wiedmann-Franz law. The term κ' is an approximation of the true thermal conductivity and generally $\kappa' \approx \kappa$. It is now possible to calculate all the components of the thermoelectric figure-of-merit.¹²

$$\sigma = \frac{ne^2 \tau(E_f)}{m}, \text{ [Eqn: 29]}$$

$$S = -\frac{\pi^2 k_B^2}{3e} \frac{\partial}{\partial E} \ln [E^{1/2} \tau(E)]_{E=\mu}, \text{ [Eqn: 30]}$$

$$\kappa' = \frac{\pi^2 k_B^2}{3e^2} \sigma T, \text{ [Eqn: 31]}$$

All thermoelectric properties reported here were calculated with BoltzTraP, a code developed by Georg Madsen and David Singh.³⁹ The remainder of Chapter 2 will reveal some of the specifics concerning the algorithms used by BoltzTraP. As seen in equation 32, an electric current under the influence of an electric field, magnetic field, and temperature gradient can be written in terms of general conductivity tensors;

$$j_i = \sigma_{ij} E_j + \sigma_{ijk} E_j B_k + v_{ij} \nabla_j T, \quad [Eqn: 32]$$

Where j_i is the i^{th} component of the electric current, σ_{ij} and σ_{ijk} are general conductivity tensors, and v_{ij} is the group velocity. E , B , and $\nabla_j T$ are the external electric field, magnetic field and temperature gradient, respectively. Two of the conductivity tensor components that directly utilize the band structure data from a DFT calculation are the group velocity and inverse mass tensor respectively;

$$v_\alpha(i, \vec{k}) = \frac{\partial \varepsilon(i, \vec{k})}{\hbar \partial k_\alpha}, \quad [Eqn: 33]$$

$$M_{\beta\mu}^{-1}(i, \vec{k}) = \frac{\partial^2 \varepsilon(i, \vec{k})}{\hbar^2 \partial k_\beta \partial k_\mu}, \quad [Eqn: 34]$$

Equation 33 is related to the slope of the energy bands $\varepsilon(i, \vec{k})$, and equation 34 is related to the energy band dispersion.

$$\sigma_{\alpha\beta}(i, \vec{k}) = e^2 \tau v_\alpha(i, \vec{k}) v_\beta(i, \vec{k}), \quad [Eqn: 35]$$

$$\sigma_{\alpha\beta\gamma}(i, \vec{k}) = e^3 \tau^2 \zeta_{\gamma uv} v_\alpha(i, \vec{k}) v_\beta(i, \vec{k}) M_{\beta u}^{-1}, \quad [Eqn: 36]$$

Here e is the charge of an electron, τ is the relaxation time within RTA, and $\zeta_{\gamma uv}$ is the Levi-Civita symbol.⁴⁶ The Levi-Civita symbol states that if any of the indexes (γ, u, v) are equal, $\zeta_{\gamma uv}$ equals zero otherwise ± 1 depending on the direction of the permutation. The

transport tensors are then calculated from the conductivity distributions $f_\mu(T, \varepsilon)$ determined by the Boltzmann transport equation;

$$\sigma_{\alpha\beta}(T; \mu) = \frac{1}{\Omega} \int \sigma_{\alpha\beta}(\varepsilon) \left[-\frac{\partial f_\mu(T; \varepsilon)}{\partial \varepsilon} \right] d\varepsilon, \quad [Eqn: 37]$$

$$v_{\alpha\beta}(T; \mu) = \frac{1}{eT\Omega} \int \sigma_{\alpha\beta}(\varepsilon) (e - \mu) \left[-\frac{\partial f_\mu(T; \varepsilon)}{\partial \varepsilon} \right] d\varepsilon, \quad [Eqn: 38]$$

$$\kappa_{\alpha\beta}^{elec}(T; \mu) = \frac{1}{e^2 T \Omega} \int \sigma_{\alpha\beta}(\varepsilon) (e - \mu)^2 \left[-\frac{\partial f_\mu(T; \varepsilon)}{\partial \varepsilon} \right] d\varepsilon, \quad [Eqn: 39]$$

$$\sigma_{\alpha\beta\gamma}(T; \mu) = \frac{1}{\Omega} \int \sigma_{\alpha\beta\gamma}(\varepsilon) \left[-\frac{\partial f_\mu(T; \varepsilon)}{\partial \varepsilon} \right] d\varepsilon, \quad [Eqn: 40]$$

where κ^{elec} is the electronic part of thermal conductivity, μ is the chemical potential, Ω is a volume element, and f_μ is the distribution function. Once these values are obtained the Seebeck and Hall coefficients are calculated;

$$S_{ij} = E_i (\nabla_j T)^{-1} = (\sigma^{-1})_{\alpha i} v_{\alpha j}, \quad [Eqn: 41]$$

$$R_{ijk} = \frac{E_j^{ind}}{J_i^{appl} B_k^{appl}} = (\sigma^{-1})_{\alpha j} \sigma_{\alpha\beta k} (\sigma^{-1})_{i\beta}, \quad [Eqn: 42]$$

Therefore, once a relaxation time is chosen and the conductivity tensors have been calculated all the components of the thermoelectric figure-of-merit, $ZT = \sigma S^2 T / (\kappa_e + \kappa_l)$ are available except the lattice component of thermal conductivity. The lattice thermal conductivity can be calculated through molecular dynamics calculations or chosen from literature. Because of time constraints all values for κ_l have been the result of literature research. As will be seen in the following sections, the choice of κ_l is highly influential on ZT . The influence of κ_l on ZT is significant for ZnO, because lattice thermal conductivity accounts for ~90% of the total thermal conductivity.^{9, 10}

CHAPTER 3

THERMOELECTRIC PROPERTIES OF SILICON

3.0 Silicon

Before the thermoelectric properties of unexplored systems can be determined the methodology must be benchmarked. It was chosen to compare the thermoelectric properties of bulk silicon against those reported by Grossmann *et al.* and the silicon NWs against the findings of Giulia Galli *et al.*^{27, 31} The structural files for the silicon NW calculations are provided by Dr. Denis Demchenko of Virginia Commonwealth University. Dr. Denis Demchenko, Dr Byounghak Lee of Texas State University-San Marcos, and I separately calculated the thermoelectric properties of the same three Silicon NWs and compared results, testing the methodology, code, and computer systems.

Differences between the thermoelectric properties reported here and those reported by Giulia Galli *et al.* are due the choice of relaxation time and surface termination. As will be discussed in a subsequent paragraph, the relaxation time used in this study is found through similar methods as reported by Galli *et al.* Although the methodology for determining τ was reported the actual value was not, therefore it is uncertain whether the same values are used here. The present study employs a single hydrogen atom termination for each dangling bond, while Galli *et al.* used a canted SiH₂

molecule for surface termination.³¹ Despite these differences, the same trends reported by Galli *et al.* are expected in this study.

3.0 Thermoelectric Properties of bulk silicon

All electronic structure calculations reported in this chapter are performed within the generalized-gradient approximation (GGA) of Perdew, Burke, and Ernzerhof (PBE),⁴⁴ with the projector-augmented wave method (PAW),⁴⁷ as implemented in the Vienna Ab-initio Simulation Package, VASP.³⁶⁻³⁸ All calculations for bulk silicon are carried out on a rectangular 8-atom simulation cell. A gamma-centered k-point sampling mesh containing 455 points in the irreducible Brillouin zone (IBZ) and an energy cutoff of 245.3 eV is used for all Si bulk calculations. The orthogonal cell and the dense k-point mesh are a requirement of the Boltzmann transport code, BoltzTraP.³⁹

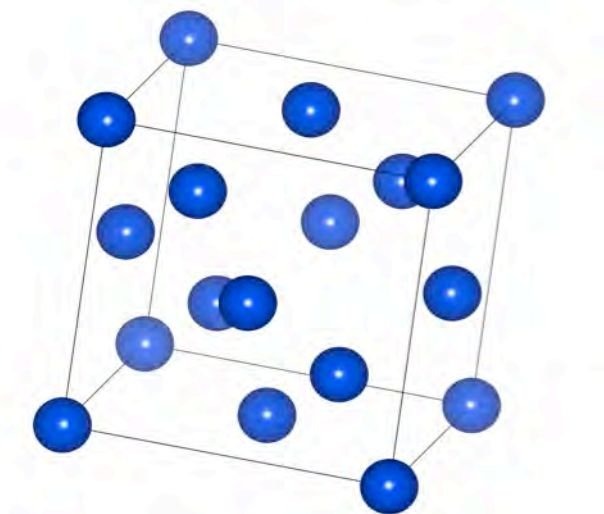


Figure 9. Conventional Unit Cell of Silicon. The minimum energy lattice constant, a , was found to be 5.47 Å. That is 0.7% more than the experimental value of 5.43 Å.

For a given lattice parameter, a , the atomic positions are optimized to correspond to the lowest total energy, E . A series of self-consistent calculations is then carried out for varying lattice parameters. Each calculation offers a data point $E(a)$. These points

were then fit to a parabola and to find the ground-state energy lattice parameter and its predicted ground-state energy. The ground-state energy calculated during the self-consistent calculation of the minimum energy structure was found to be -5.41419 eV/atom, a difference of 0.001% from the predicted value of -5.41413 eV/atom. The small difference between the predicted and calculated ground-state energy reveals that the parabola of the form $E=1+aa+\beta a^2$ provides an accurate fit to the data points $E(a)$. The calculated lattice parameter, $a=5.47 \text{ \AA}$, is 0.7% larger than the experimental value of 5.43 \AA . The minimum energy lattice parameter was then used to calculate the ground-state electronic structure of bulk silicon. Both the density-of-states and band calculation require charge density information from a converged self-consistent calculation.

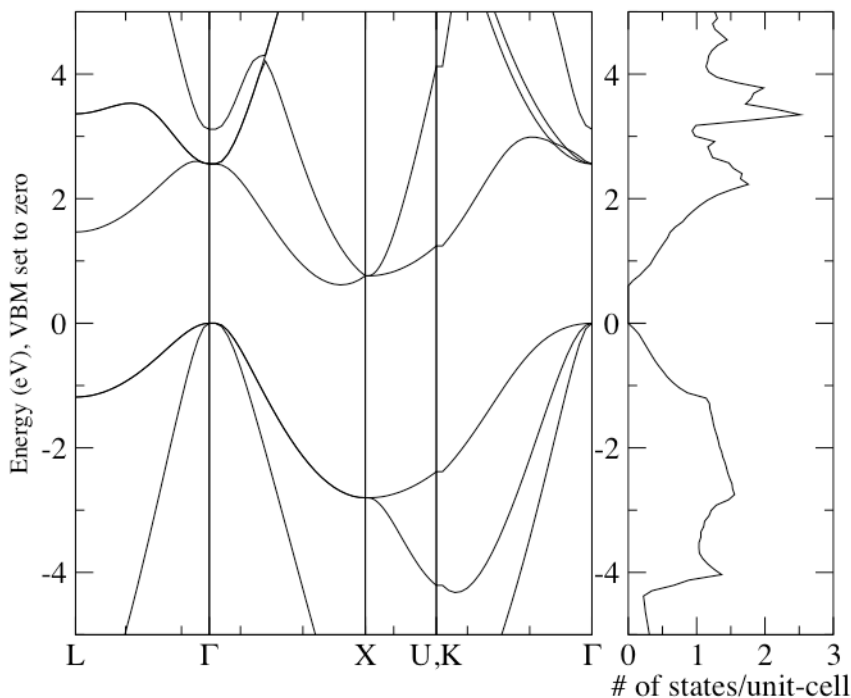


Figure 10. Electronic Structure of Si Bulk; calculated ground-state lattice parameter of 5.47 \AA . The band gap was found to be 0.616 eV , nearly half of the experimental value of 1.1 eV . In general, band gap values calculated within LDA/GGA are smaller than experimental values because LDA/GGA overestimates orbital interactions.

Next the band structure and the density-of-states is calculated using the charge density from a converged, self-consistent calculation. During the band structure and DOS calculations the charge density is not updated, not self-consistent. By subtracting the highest valence band energy value from the lowest conduction band energy value the band gap can be obtained. As seen in Figure 10 the band gap of bulk silicon was determined to be 0.616 eV, nearly half of the experimental value, 1.1 eV. The underestimation of the band gap is an intrinsic flaw of the LDA/GGA density functional theory.

Although the band gap is underestimated, the band dispersion and basic trends reflect experimental band structure. For comparison, the band gaps of the Si NWs will be compared with the band gap of bulk silicon calculated in this study, 0.616 eV. The thermoelectric properties, as describes by Boltzmann theory, are only dependent on the band dispersion, and not the band gap. For this reason there is no need to provide any band gap correction scheme to the electronic structure calculation.

The thermoelectric properties of bulk silicon were calculated from the energy eigenvalues of a self-consistent DFT calculation. Both the upper valence bands and lower conduction bands are included in the calculation, however all values reported are for the conduction band electrons. The energy interval ($\epsilon_F = -0.4$ Rydberg, $\epsilon_F = +0.4$ Rydberg) was used to evaluate the integrals in Eqn. 37 thru Eqn. 40. The interval was intentionally set large to reduce the chance of missing any bands when calculating wide band gap semiconductors. The step size of the sampling grid is 0.0005 Ry (0.0068 eV). The energy range for the chemical potential is .15 Ry (2.0408 eV) around the Fermi level. The temperature range of interest for all transport calculations is 0 K to 800 K with a step

size of 50 K. The relaxation time (τ) for different carrier concentrations was found by fitting the calculated mobility with the measured value.⁴⁸ The best fit is described by the following;

$$\tau(n) = \tau_{\min} + \frac{(\tau_{\max} - \tau_{\min})}{1 + n\alpha}, \quad [\text{Eqn: 43}]$$

where $\tau_{\min}=1.44913$, $\tau_{\max}=8.03289$, $\alpha=1.89859$, and n is the carrier concentration. The relaxation times found for bulk silicon are also used in the calculations for silicon NWs.

The choice of lattice thermal conductivity is highly influential on the thermoelectric figure-of-merit. The lattice component of thermal conductivity of bulk silicon at 300 K is reported experimentally to be 100 W/Km⁴⁹, 116 W/Km⁵⁰, and 124 W/Km⁵¹. To be consistent with Grossman *et al.* a value of 100 W/Km is used in the bulk silicon calculations. A lattice thermal conductivity of 100 W/Km results in a thermoelectric figure-of-merit ~ 0.007 , 35% smaller than the experimental value of $ZT=0.01$.²⁵ For comparison, we show ZT for the lattice thermal conductivity of 80 W/Km in Figure 11 (d).

It was found that when lattice thermal conductivity was 100 W/Km bulk silicon has a maximum ZT of ~ 0.007 , optimized at a carrier concentration of $9 \times 10^{19} \text{ cm}^{-3}$. The calculated electrical conductivity optimized at a value of $1440 (\Omega\text{cm})^{-1}$ at a carrier concentration of 10^{20} cm^{-3} . This is on the same order of magnitude as that reported by Grossman *et al.*, $2080 (\Omega\text{cm})^{-1}$ at the same concentration.²⁵ The electronic component of thermal conductivity in this study was found to be 1.54 W/Km at a carrier concentration of 10^{20} cm^{-3} . That is 0.39 W/Km larger than the value reported by Grossman *et al.* They also reported a Seebeck coefficient of -0.290 mV/K at a concentration of 10^{19} cm^{-3} that increases linearly to -0.12 mV/K at 10^{20} cm^{-3} . The results found here follow a similar

trend; a Seebeck coefficient of -0.323 mV/K at 10^{19} cm $^{-3}$ that increased linearly to a value of -0.13 mV/K at 10^{20} cm $^{-3}$. The differences between the values reported By Grossman *et al.* those reported here can be attributed to the choice of τ .

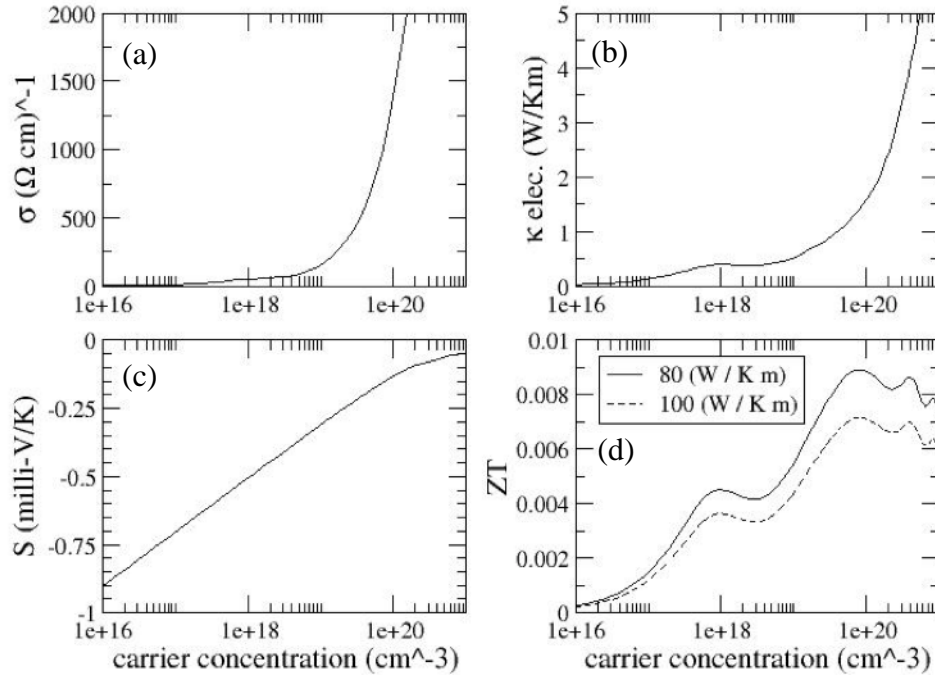


Figure 11. Thermoelectric Properties of Si Bulk 8-atom Cell at 300 K. (a) electrical conductivity σ , (b) Electronic component of thermal conductivity κ_e , (c) Seebeck coefficient S , (d) thermoelectric figure-of-merit, ZT for 300 K. Lattice thermal conductivity κ_l was taken to be 100 and 80 W/Km, represented by dashed and solid lines respectively. The relaxation time τ was determined by fitting the mobility to measured carrier concentration dependent mobility data. As reportedly done by Galli *et al.*

3.2 Thermoelectric Properties of Silicon Nanowires

Three hydrogen-passivated silicon NWs with diameters of ~ 11 Å, but of different growth directions were chosen as the systems to be benchmarked against because similar calculations have been reported by Galli *et al.*²⁷ The NWs were constructed from bulk silicon with the NW's axis parallel to the growth direction of interest. A radius is then chosen to define an imaginary cylinder. All the atoms outside the cylinder are discarded, while all the atoms inside are preserved. The dangling bonds on the bare silicon NW are

then repaired by terminating each bond with hydrogen atoms. The H-Si bond length is half of the original Si-Si bond length, but the Si bulk bond angle is preserved. This provides a simple and effective method of eliminating surface states in the electronic structure.

Figure 12 shows the cross section of the three silicon NWs. The [001], [011], and the [111] NWs have diameters of 11, 11.6, and 11.6 Å respectively. The [001] has 65, [011] has 42, and [111] has 104 atoms per simulation cell. The optimized lattice parameter for bulk, $a=5.47$ Å, was utilized for the structure of the wire. The simulation cells are rectangular and accommodate ~ 3.5 Å thick vacuum perpendicular to the growth direction encapsulating the NW, resulting in ~ 7 Å of vacuum between each NW. This is to prevent any interaction between the NWs. The three NWs were fully relaxed until the force on each atom was less than 0.001 eV/atom. Figure 13 represents the silicon NW oriented in the [001] direction, from the perspective of looking down the [100] direction of the simulation cell.

The relaxations were carried out with an energy cutoff of 245.3 eV and a gamma-centered k-point sampling mesh of $4 \times 4 \times 24$. This results in 78, 117, and 150 k-points in the irreducible Brillouin zone (IBZ) for the [001], [011], and the [111] NWs, respectively. The relaxed structures were then determined within a self-consistent calculation, by allowing the charge density data to update with each iteration. The charge density from this self-consistent calculation is then used to determine the band structure and density-of-states.

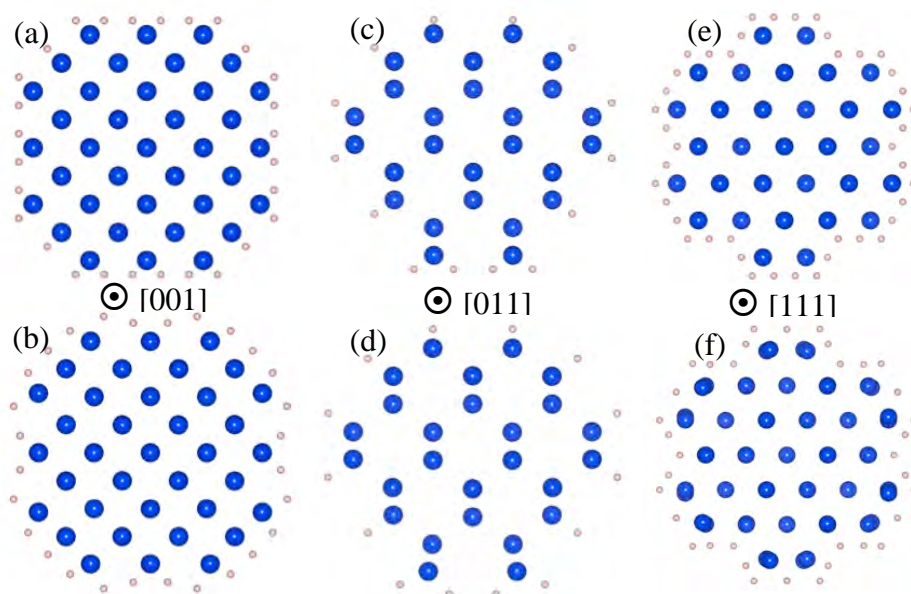


Figure 12. Cross Section of Si Nanowires; (a) and (b) represent the [001]-nanowire, ideal and relaxed. (c) and (d) the [011]-nanowire, ideal and relaxed. (e) and (f) the [111]-nanowire, ideal and relaxed. All three wires roughly ~ 10 Å. Blue represents Si and beige H-termination. Ideal structure files provided by Denis Demchenko of VCU.

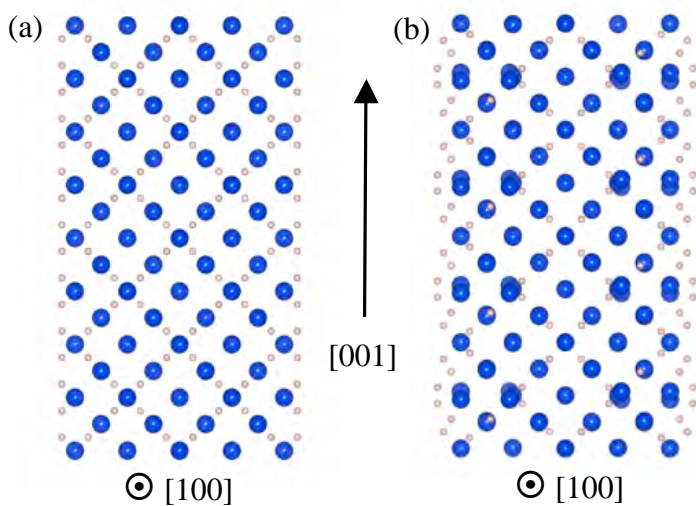


Figure 13. Si NWs Oriented in the [001] Direction. (a) and (b) are the ideal and relaxed structure, respectively. The H-termination can be seen well in (a). The profile shows the two broken bonds capped with a hydrogen atom for each silicon atom on the surface. H atoms are beige, Si atoms are blue.

Figure 14 is the electronic structure for the H-passivated silicon NW oriented in the [001] direction with a diameter of 11 Å. The effects of quantum confinement on the band gap can be seen in the dramatic increase from bulk to NW, 0.616 to 2.124 eV. Galli *et al.* reported a value of 2.35 eV for the same diameter and orientation, but different surface termination schemes (SiH₂ vs. H). The [011] oriented NW with a diameter of 11.6 Å was found to have a band gap of 1.398 eV. The value calculated is 0.322 eV smaller than what was reported by Galli *et al.* A band gap of 1.849 eV was found for the [111] oriented NW, 0.271 eV smaller than what was reported by Galli *et al.*²⁷

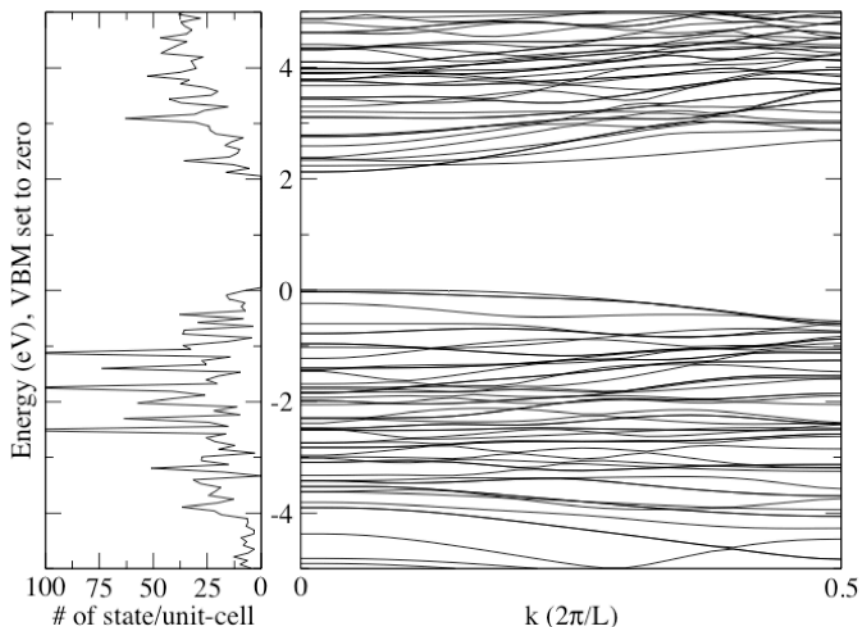


Figure 14. Electronic Structure of the [001] Si NW. The [001] NW has a diameter of 11 Å and contains 65 atom/simulation cell. The band gap was found to be 2.124 eV, a factor of ~3.48 larger than the calculated band gap of bulk silicon, 0.616 eV. Despite a different surface termination techniques, Galli *et al.* reported a value of 2.35 eV for the same diameter wire and orientation.

It was reported by Galli *et al.* that the conduction band of the silicon NW oriented in the [011] direction has the smallest conduction band effective mass with a value of $0.14 \times m_e$, while the [001] and [111] have values of $0.72 \times m_e$ and $4.78 \times m_e$ respectively.³¹ As seen in Figures 14-16, the electronic structure calculated here for the [011] has the

smallest conduction band effective mass and smallest band gap compared with the [001] and [111] oriented NWs.

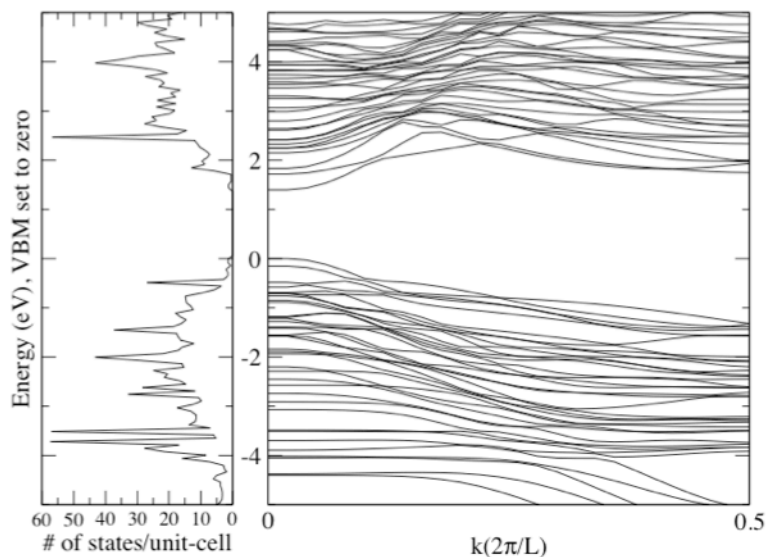


Figure 15. Electronic Structure of the [011] Si NW. The [011] NW has a diameter of 11.6 Å and contains 42 atom/simulation cell. The band gap was found to be 1.398 eV, a factor of ~2.3 larger than the calculated band gap of bulk silicon, 0.616 eV. Galli *et al.* reported a value of 1.72 eV for the same diameter wire and orientation.

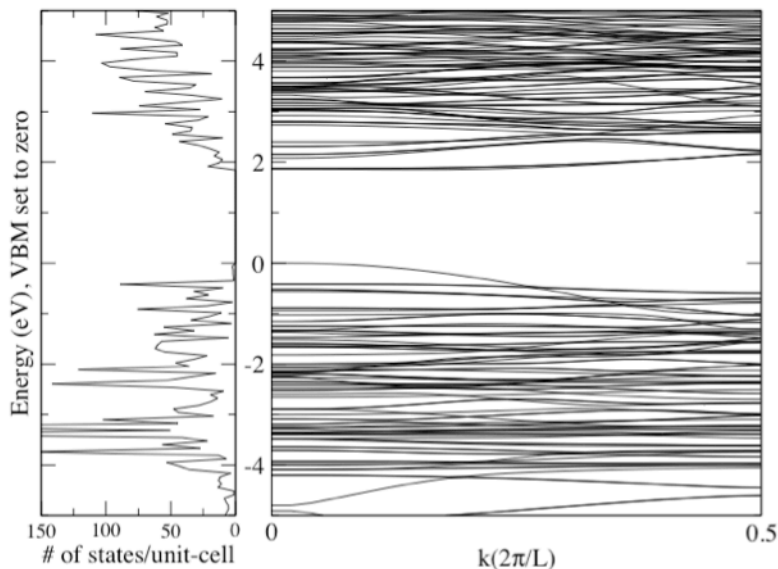


Figure 16. Electronic Structure of the [111] Si NW. The [111] NW has a diameter of 11.6 Å and contains 104 atom/simulation cell. The band gap was found to be 1.849 eV, a factor of ~3 larger than the calculated band gap of bulk silicon, 0.616 eV. Galli *et al.* reported a value of 2.12 eV for the same diameter wire and orientation.

The difference between the electronic structure in this study and others can be attributed to the choice of surface termination. Instead of terminating each dangling bond with one hydrogen atom, as done in the present calculations, Galli *et al.* used a canted silicon dihydride (SiH_2) molecule.³¹ The relationship between wire diameter and the size of the band gap is well documented for Si and other materials. For most NWs the effects of quantum confinement become quite apparent when diameters approach $\sim 30 \text{ \AA}$ and the band gap begins to depart from the bulk value. As the diameter decreases further below $\sim 30 \text{ \AA}$ the band gap dramatically increases.³¹⁻³³

The thermoelectric properties of the silicon NWs are then calculated from the electronic structure determined by DFT. The calculations for the NWs were carried out with the same sampling settings and temperature range as utilized for bulk. Both the upper valence bands and lower conduction bands are included in the calculation, however all values reported are for the conduction electrons. The same parameters for the thermoelectric calculation used for bulk are used for the NWs. The relaxation time used in the calculation of bulk silicon is also adopted for the silicon NWs. Refer back to the discussion on bulk silicon for more information. The lattice thermal conductivity of the NWs is the same as used by Galli *et al.*, 2 W/Km , determined by molecular dynamics calculations.

Due to the difference in choice of surface termination and relaxation time the values for the thermoelectric properties calculated in this study do not compare well with those reported by Galli *et al.* (see Fig. 7), but the basic trends share similar characteristics. The electrical conductivity of bulk silicon is higher than any of the NWs. As reported by Galli *et al.*, the [011] growth direction 11.6 \AA diameter NW calculated

here has the highest electrical conductivity. The results of this study found an electrical conductivity of $185 (\Omega\text{cm})^{-1}$ at a carrier concentration of $4 \times 10^{19} \text{ cm}^{-3}$ for the [011], ~40 times less than what was reported by Galli *et al.*, $7500 (\Omega\text{cm})^{-1}$ at $4 \times 10^{19} \text{ cm}^{-3}$.

The electronic component of thermal conductivity reported in this study also follows the same trend as Galli *et al.*, but the values are again in disagreement. The [011] is found to have the highest thermal conductivity of 0.48 W/Km, followed by the [001] (0.33 W/Km) and the [111] (0.13 W/Km). These values are approximately 1/2 of what was reported by Galli *et al.* (see Fig. 7). This discrepancy is most likely the result of the different relaxation time values used in the separate calculations. Unfortunately literature research into the effects of the different surface termination schemes on phonon scattering for NWs has yielded no results.

Before considering the effects of thermal conductivity, the thermopower ($S^2\sigma$) of the silicon NWs is investigated. It is known that a high thermopower often correlates with a sharp peaks in the electronic density of states at the Fermi level. The results of these calculations can be seen in Figure 17. The [001] has both the steepest peak at the Fermi level and the highest thermopower of all three wires. The [001] has a thermopower of $0.62 \text{ mW/K}^2\text{m}$ at a carrier concentration of $1.16 \times 10^{20} \text{ cm}^{-3}$. The [111] has a thermopower of $0.5 \text{ mW/K}^2\text{m}$ at a carrier concentration of $4.9 \times 10^{20} \text{ cm}^{-3}$. The highest peak in the thermopower of the [011] was optimized at a carrier concentration of $3 \times 10^{19} \text{ cm}^{-3}$ at a value of $0.46 \text{ mW/K}^2\text{m}$.

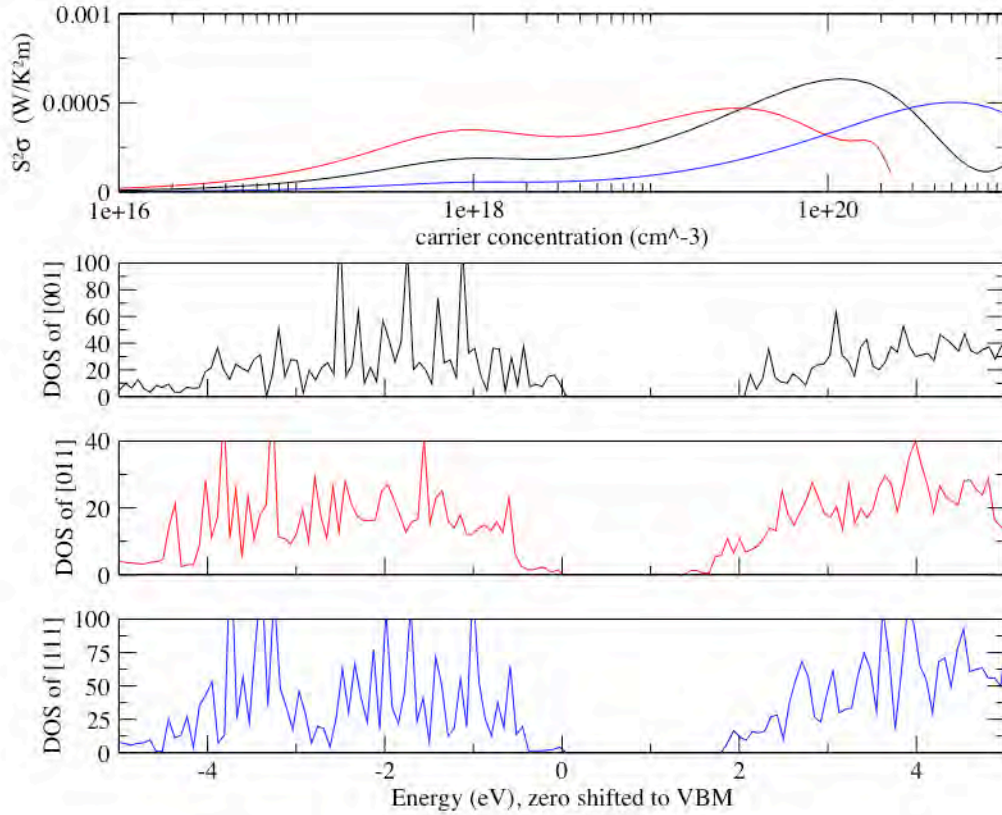


Figure 17. Thermopower, $S^2\sigma$, of Si NWs at 300 K; (a) Thermopower of the 3 silicon NWs. The [001] is represented in black, the [011] in red, and the [111] in blue. (b) The electronic density of states for the [001], (c) the DOS for the [011], (d) and the DOS for the [111]. An increase in the thermopower is related to the DOS at the fermi level. A steep peak in the DOS correlates with a high $S^2\sigma$.

Because of the differences between the components of the thermoelectric figure-of-merit calculated in this study and those calculated by Galli *et al.* it is safe to assume values for ZT will also not compare well. The carrier concentrations that optimize ZT for each NW are similar but the maximum value ranking is different. It was reported by Galli *et al.* that the [001] has the highest thermoelectric figure-of-merit ($ZT=2.5$) followed by [011] ($ZT=2$) and [111] ($ZT=1.6$). The results of this study show that the [001] ($ZT=0.08$) is the highest at a carrier concentration of $1.07 \times 10^{20} \text{ cm}^{-3}$ followed by the [111] ($ZT=0.065$) at a carrier concentration of $4.6 \times 10^{19} \text{ cm}^{-3}$ and [011] ($ZT=0.06$) at a carrier concentration of $2.8 \times 10^{19} \text{ cm}^{-3}$.

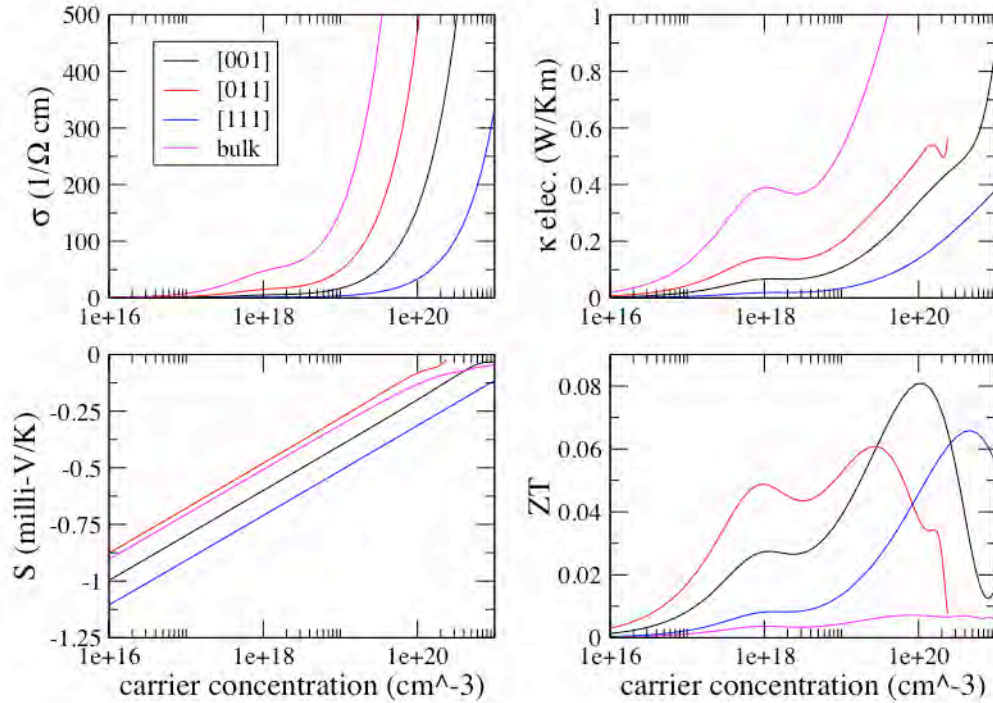


Figure 18. Thermoelectric Properties of Si NWs at 300 K Calculated with BoltzTraP; (a) electrical conductivity σ , (b) electronic thermal conductivity $\kappa_{elec.}$, (c) Seebeck coefficient S , (d) thermoelectric figure-of-merit ZT . Relaxation was found by fitting bulk mobility data. The lattice component of thermal conductivity for silicon NWs as reportedly used by Galli *et al.*, $\kappa_l=2$ W/Km. For bulk $\kappa_l=100$ W/Km.

The values calculated in this study and those reported by Galli *et al.* are significantly different but most of the overall trends remain similar. Attempting to reproduce the results for the silicon NWs has provided confidence in the employed methodology. The thermoelectric figure-of-merit calculated for bulk silicon with a electronic component of thermal conductivity of 100 W/Km compared reasonably well with the experimental value, $ZT_{Si\ bulk} \approx 0.01$.^{25, 33} The same results found in this study were also calculated by Dr. Denis Demchenko and Dr. Byounggak Lee. This provides assurance that if the same methodology used for bulk was used for the NWs accurate results can be expected. Galli *et al.* did not report any bulk calculations so it is unclear if

their methodology will result in ZT values comparable with what is found experimentally.

Although not the extraordinary increase reported by Galli *et al.*, the present calculations does find the ZT of silicon NWs to be ~10 times that of the calculated ZT of bulk silicon, from $ZT=0.007$ to 0.08. If the experimental value of $ZT_{Si\ bulk}=0.01$ is assumed for bulk then Galli *et al.* reported a maximum of ZT 2.5, that is an increase of 250 times over bulk silicon (see Fig. 7). The main contribution to this discrepancy is the differences in the calculated electrical conductivities. As seen in equation 6 ($ZT=(S^2\sigma/\kappa)T$), ZT is directly proportional to σ . Therefore if σ is ~40 larger, ZT is expected to be at least one order of magnitude larger.

CHAPTER 4

THERMOELECTRIC PROPERTIES ZINC OXIDE NANOWIRES

4.0 Zinc Oxide

Zinc oxide exists in three crystal structures; wurtzite, zinc blende, and rocksalt. In ambient conditions the most stable phase of ZnO is wurtzite. The zinc blende and rocksalt structures can be achieved through growth on cubic substrates or the introduction of high pressure, respectively.⁵² For the present study only the wurtzite phase of ZnO will be considered. Wurtzite is indexed by Strukturbericht designation – B4, space group – $P6_3mc$, and number 186. The primitive cell is non-orthogonal, with an angle of 120° between lattice vectors a and b . X-ray diffraction experiments report that the room temperature lattice vectors a , c , and the unit less basis parameter u to be 3.253\AA , 5.213\AA and 0.382 respectively.⁵³ The basis parameter u times c , uc , defines the inter-planer spacing in the $[001]$ direction between atoms of opposite species.

First the bulk crystal structure is optimized for the lowest energy configuration. Then the electronic structure of Bulk ZnO is calculated using the relaxed optimized structure. The thermoelectric properties of Bulk ZnO are then calculated from the band structure determined by a converged DFT calculation. After the Bulk ZnO thermoelectric properties are calculated the ZnO NWs are constructed and each is optimized to obtain the minimum energy structure. The minimum energy structure is then used to calculate the ground-state band structure and DOS. The band structure data

from a converged self-consistent calculation can then be used to calculate the thermoelectric properties of ZnO NWs.

4.1 Thermoelectric Properties of Zinc Oxide Bulk

The structural optimization and electronic structure calculations discussed in this chapter are carried out on the four-atom, hexagonal simulation cell. The first step is to find the minimum energy crystal structure of ZnO with the aid of density functional theory. The structural optimization is carried out using the generalized-gradient approximation (GGA) in the form of Perdew-Burke-Ernzerhof (PBE)⁴⁴ within the projector-augmented wave method (PAW)⁴⁷. A gamma-centered k-point grid of 11x11x11 and an energy cutoff of 400 eV are used for the structural optimizations. The minimum energy configuration is then determined by running a series of DFT calculations. In each case a different structural input file is generated, sampling points (a_i, c_j, E_{ij}) around the known experimental lattice parameters. Each structure is then allowed to relax, without any constraints, until the forces between each atom are below 0.001 eV/Å. Each relaxed structure, characterized by different values for the lattice parameters a and c , has a corresponding ground-state energy value. A 4th degree polynomial [see Equation 43] is used to fit a surface to the data points, (a_i, c_j, E_{ij}) . The function that defines the surface (see Eqn: 43) was then minimized to find the lowest energy configuration for lattice parameters a and c .

$$E_0(a, c) = 1 + \eta_1 a + \eta_2 a^2 + \eta_3 c + \eta_4 c^2 + \eta_5 ac + \eta_6 a^2 c + \eta_7 ac^2 + \eta_8 a^2 c^2, \quad [\text{Eqn: 44}]$$

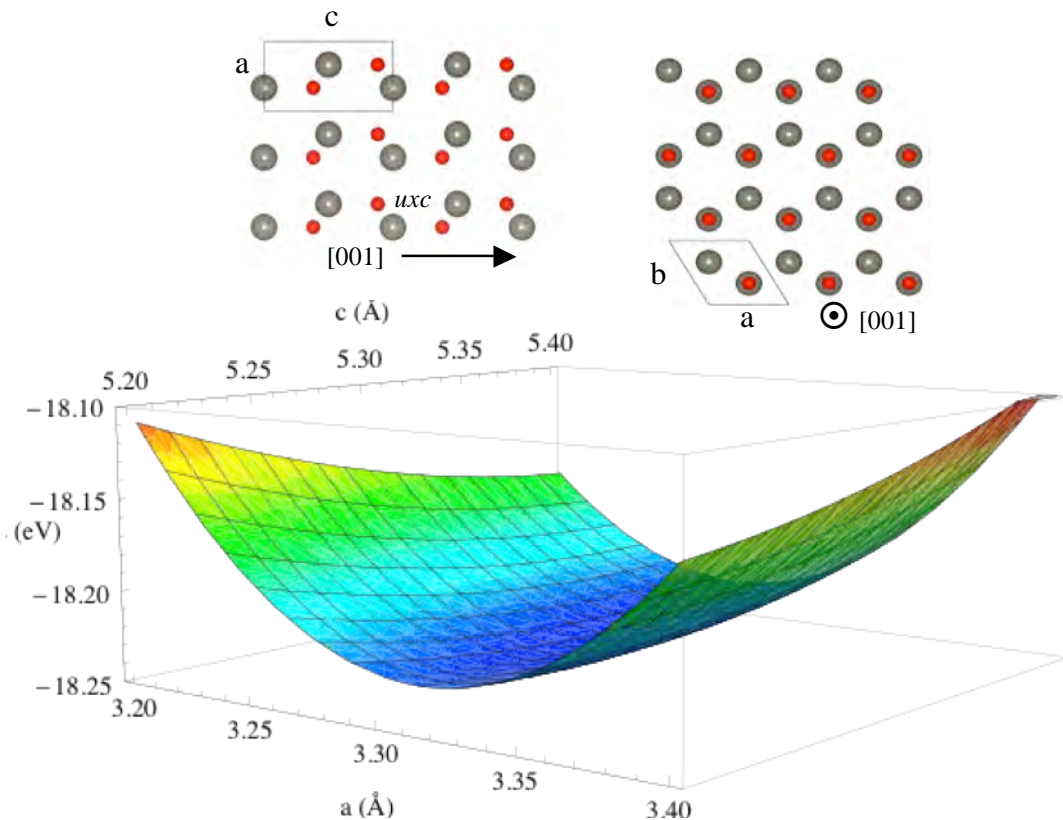


Figure 19. Minimum Energy Surface of Bulk ZnO. Energy versus lattice parameters a and c . The energy has been scaled such that the darker color corresponds to a lower ground-state energy value. This data was fit to a polynomial of the fourth-order and the surface function was minimized. All DFT calculations are carried out within PAW-PBE on a 4 atom non-orthogonal unit cell. The minimum of this surface was found to be at; $a = 3.29406 \text{ \AA}$ and $c = 5.30796 \text{ \AA}$. After a convergence test was carried out a gamma centered k-point grid with dimensions of $11 \times 11 \times 11$ was determined sufficient.

With the settings and methods discussed in the preceding paragraph; a , c , and u are found to be 3.294 \AA , 5.308 \AA , and 0.382 respectively (see Fig. 19). With these parameters the predicted ground-state energy per atom of the relaxed, wurtzite-phase bulk ZnO is $-4.558975 \text{ eV/atom}$. The calculated value for the ground-state energy per atom of the minimum energy structure is found to be $-4.558551 \text{ eV/atom}$, a difference of 0.009% . The small difference between the predicted and the calculated ground-state energy/atom assures that the 4th order polynomial provides a precise fit. The ground-state energy

structure overstates the lattice constants compared to experimental RT measurement by 0.041 Å and 0.094 Å for a and c respectively.⁵⁴ Other DFT calculations have reported the lattice parameters to be; $a=3.289$ and $c=5.315$ Å,⁵⁵ $a=3.292$ and $c=5.309$ Å,⁵⁶ $a=3.24$ and $c=5.1905$ Å.⁵⁷ Once the ground-state lattice parameters are established, the band structure and density-of-states can be calculated. The minimum energy surface is illustrated in Figure 19. The RGB color scale is such that the dark blue represent low energy values for given lattice parameters a and c .

<u>Source</u>	<u>a (Å)</u>	<u>c (Å)</u>	<u>u</u>
experimental; x-ray diffraction (ref.59)	3.253	5.213	0.382
this work	3.294	5.308	0.382
DFT (ref. 60)	3.289	5.315	na
DFT (ref. 61)	3.292	5.309	0.3793
DFT (ref. 14)	3.24	5.1905	0.382

Table 1. ZnO Lattice Parameters. The lattice parameters determined in this work correlate well with other DFT values.

The band structure and density-of-states of Bulk ZnO are then calculated from the ground-state charge density. The electronic structure is determined with a gamma-centered k-point mesh of 11x11x11 and an energy cutoff of 400 eV. The band structure and density-of-states (electrons/unit cell) of Bulk ZnO can be seen in Figure 21 and Figure 20, respectively. The upper panel of Figure 20 compares the total DOS with the contribution from each species of atom, revealing the contributions of all the atomic orbitals, for every atom of a given species used in the simulation cell. The lower two panels of Figure 20 split the contribution to the atomic orbitals (total s, total p, and total d) for zinc and oxygen. The DOS plot shows that the highest valence bands are

composed of O p -orbitals and Zn d -orbitals. The lowest conduction bands are composed of O p -orbitals and Zn s -orbitals.

The calculated band gap for bulk ZnO is found to be 0.73 eV, 4.7 times smaller than the experimental value of 3.4405 eV.⁵⁴ The underestimation of the band gap for semiconductors and insulators is a well known problem of LDA/GGA DFT. Not only does LDA/GGA severely underestimate the band gap, but it fails to accurately describe position of the semi-core d -states, especially in II-VI semiconductors.⁵⁸⁻⁶¹

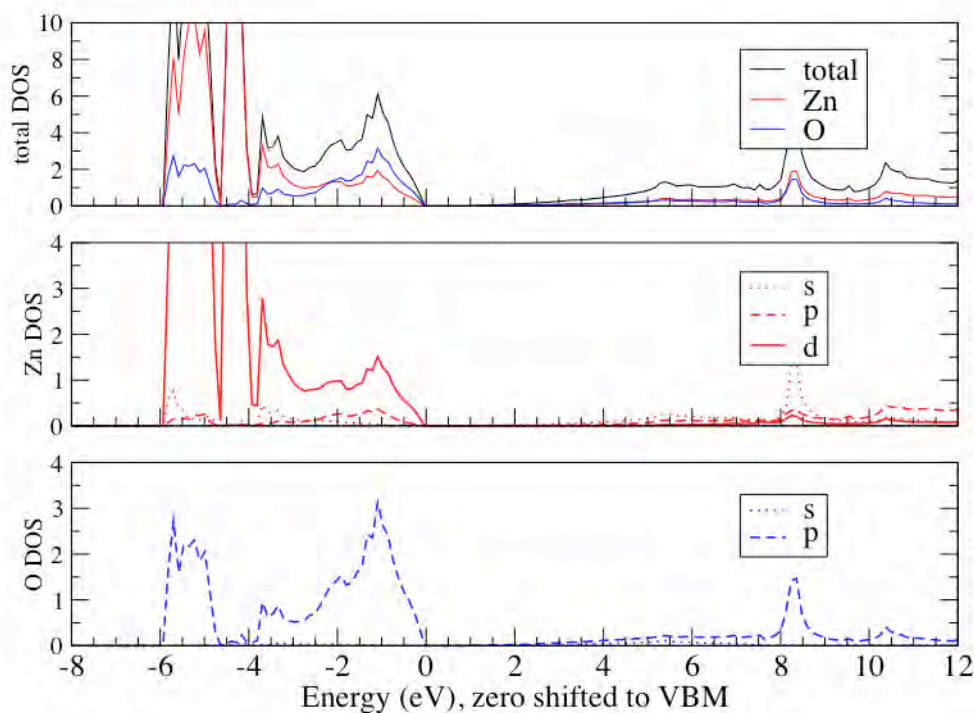


Figure 20. Density-of-States of Bulk ZnO; represented in units of number-of-electrons/simulation cell. The upper panel reveals the sum of all the orbits for the Zn and O atoms compared with the total density-of-states. The lower panels show specific orbital contribution for Zn and O. The band gap was found to be 0.73 eV. The overstated d -states can be seen in the energy range -6 to -4 eV.

According to Peter Schröer *et al.* the interaction between the oxygen p -orbitals and the zinc d -orbitals is exaggerated in standard LDA/GGA density functional theory.⁵⁸ These problems are associated with an electron's unphysical, self-interaction and its

exchange-energy; constructs of the approximations utilized by traditional LDA/GGA density functional theory. The elusiveness of these deficiencies can be removed when considering one hydrogen atom. The hydrogen atom has only one electron but DFT calculates an electron-electron interaction and an exchange energy even though there is nothing for a single electron to exchange with.⁴⁵

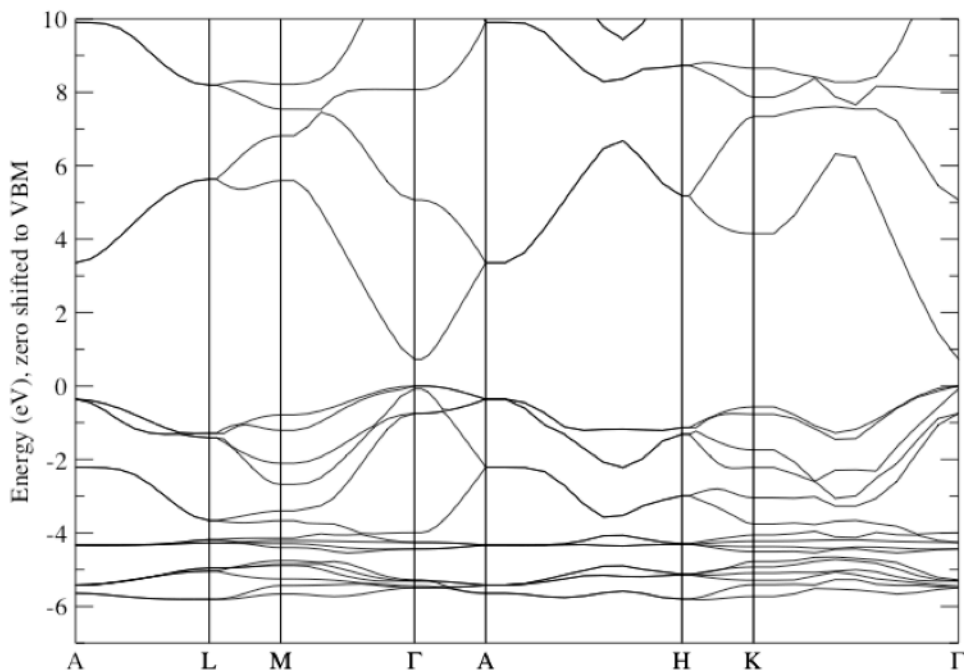


Figure 21. Band Structure of Bulk ZnO; calculated with PAW PBE pseudopotentials. The band gap was found to be 0.73 eV, considerably smaller than the experimental value of 3.4405 eV, but close to other DFT calculations, 0.75 eV. The underestimated bandgap is a well known shortcoming of LDA calculations. Similar to other II-VI LDA calculations the *d*-electron bands appears 3 eV higher than experimental data.

The calculated electronic structure data $E(n, \mathbf{k})$ are then used to determine the thermoelectric properties; electrical conductivity σ , electronic component of thermal conductivity κ_e , Seebeck coefficient S , and the thermoelectric figure-of-merit ZT . The structural optimization and calculation of the electronic structure (see figs. 18-21) utilized a gamma-centered k-point grid of 11x11x11. The electronic structure used to determine the thermoelectric properties was calculated with a grid of 24x24x24, because the

Boltzmann transport code used in this study requires a dense k-point grid. The energy interval ($\epsilon_F = -0.4$ Rydberg, $\epsilon_F = +0.4$ Rydberg) was used to evaluate the integrals in Eqn. 37 thru Eqn. 40. The interval is intentionally set large to reduce the chance of missing any states that are relevant to the thermoelectric properties. The grid size of the interpolated energy is 0.0005 Ry (0.0068 eV). The energy range for the chemical potential is 0.15 Ry (2.0408 eV) around the Fermi level of the undoped system. The temperature range of interest for all reported transport calculations is 0 K to 800 K with a step size of 50 K. Different values for the relaxation time and the lattice component of thermal conductivity will be used for Bulk ZnO and NWs.

The values used for the relaxation time τ and the lattice component of thermal conductivity κ_l of all ZnO thermoelectric calculations are the result of literature research. The thermoelectric properties of Bulk ZnO are calculated with a relaxation time τ of 30×10^{-15} sec. Literature research reveals the relaxation time τ of ~ 100 Å diameter ZnO NWs to be 30×10^{-15} sec., determined through time-resolved terahertz spectroscopy.⁶² The relaxation time values of bulk ZnO calculated from mobility data found in literature ranges from 17×10^{-15} to 57.9×10^{-15} sec for carrier concentrations on the order of $\sim 10^{16}$ cm⁻³.⁶³ Our choice of τ lies within the reported bulk value range. We use the same relaxation time for bulk and NW calculations. The difference in the overall thermoelectric properties arising from the differences in the relaxation time is believed to be small.²⁷ Because the lattice contribution to the thermal conductivity is much larger than the electronic contribution, ZT is sensitive to the choice of κ_l .^{1, 3, 14, 17, 27} This will be seen in both silicon systems and ZnO systems.

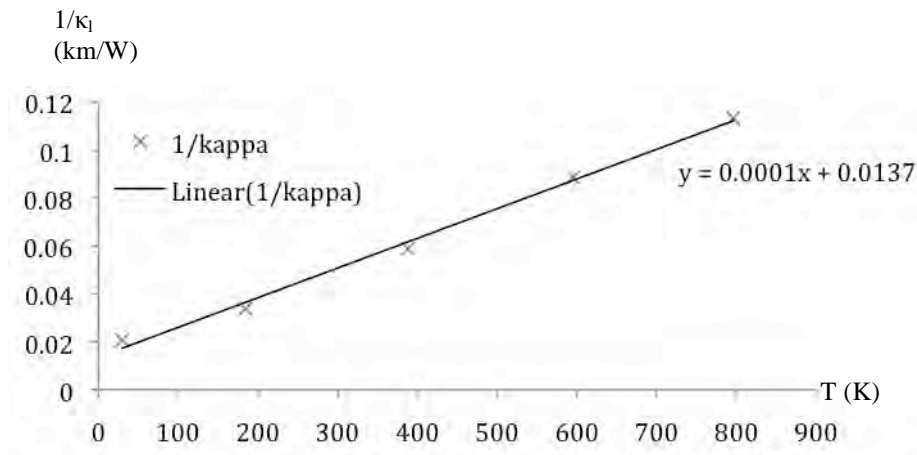


Figure 22. Lattice Component of Thermal Conductivity of Bulk ZnO; Data was digitized from the experimental results of Toshiki Tsubota *et al.* The data point for 1000 K skewed the data, so it was omitted. Lattice component of thermal conductivity was found to be 23 W/Km at 300 K, 16 W/Km at 500 K, and 12 W/Km at 700 K.

The lattice component of thermal conductivity κ_l for Bulk ZnO was determined by digitizing experimental κ_l figures determined from measured thermal diffusivity and specific heat (Figure 7 of ref. 6).¹⁰ The figure was digitized and the κ_l values were extracted, then $1/\kappa_l$ was plotted vs. temperature as seen in Figure 22. The data point for 1000 K was removed because it skewed the fitting and was located outside the temperature range of interest. The lattice component of thermal conductivity is then calculated from a linear fit of the digitized data. For 300, 500, and 700 K κ_l is calculated to be 23, 16, and 12 W/Km respectively. The figure-of-merit for bulk ZnO is evaluated with these κ_l values at their corresponding temperatures.

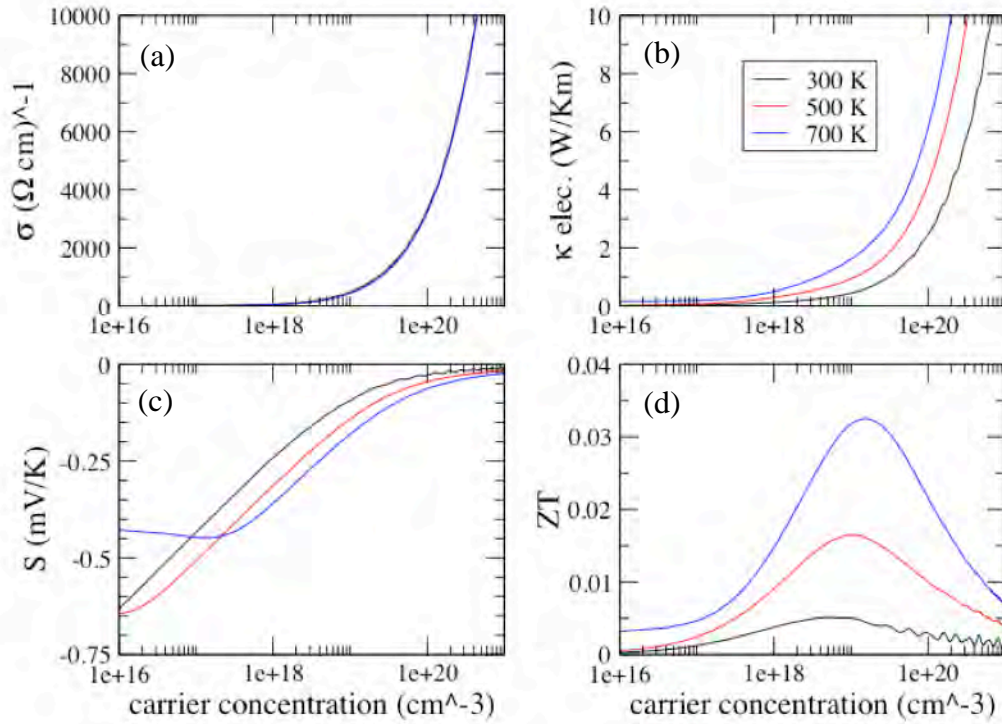


Figure 23. Thermoelectric Properties of Bulk ZnO: (a) Electrical conductivity, (b) Electronic part of thermal conductivity, (c) Seebeck coefficient, and (d) ZT. The black, red, and green lines represent 300 K, 500 K and 700 K respectively. A higher density k-point mesh of 24x24x24 was used for the self-consistent data utilized in the Boltzmann transport calculation. Different values of ZT are calculated using different values of κ lattice for each temperature corresponding to data of Tsubota *et al.* These values are; 300 K $\kappa = 23$ W/K m, 500 K $\kappa = 16$ W/K m, and 700 K $\kappa = 12$ W/K m. Relaxation time τ was chosen to be 30×10^{-15} sec.

As seen in Figure 23, the thermoelectric properties of Bulk ZnO is calculated at temperatures of 300, 500, and 700 K.. The calculated electrical conductivity is found to be roughly independent of temperature in the range of 300 to 700 K and takes a value of $3250 (\Omega \text{cm})^{-1}$ at a carrier concentration of 10^{20} cm^{-3} . This value is 77% higher than the electrical conductivity calculated for bulk silicon at 300 K. As expected, the electronic contribution to thermal conductivity is temperature dependent. The values of κ_e at a carrier concentration of 10^{20} cm^{-3} are 2.4 W/Km, 4.2 W/Km, and 6.05 W/Km for the temperatures 300, 500, and 700 K respectively. For comparison, the electronic component of thermal conductivity of bulk silicon was calculated to be 1.54 W/Km at

300 K at the same carrier concentration. The Seebeck coefficient is also temperature dependent with the highest values for a temperature of 300 K.

Analyzing only the electrical conductivity, the electronic component of thermal conductivity and the Seebeck coefficient would lead one to believe that ZT would be highest for a temperature of 300 K. However, Figure 23 illustrates the highest ZT for a temperature of 700 K as a result of a low lattice component of thermal conductivity. This demonstrates that the choice of the lattice component of thermal conductivity is highly influential on ZT. At 300 K the thermoelectric figure-of-merit is optimized at a carrier concentration of $5.5 \times 10^{18} \text{ cm}^{-3}$ with a value of 0.005. At 500 K ZT is optimized at a carrier concentration of 10^{19} cm^{-3} with a value of 0.016. At 700 K ZT is optimized at a carrier concentration of $1.6 \times 10^{19} \text{ cm}^{-3}$ with a value of 0.03. Thermoelectric properties of bulk ZnO are calculated at different temperatures to explore the temperature dependence of the thermoelectric properties. All calculations pertaining to the ZnO NWs are carried out at a constant temp of 300 K.

4.2 Thermoelectric Properties of Zinc Oxide Nanowires

The NWs are constructed from wurtzite phase Bulk ZnO by first selecting a wire axis perpendicular to the (0001). The growth direction of [0001] is chosen because experimental results from selected-area electron diffraction patterns (SAED), report the [0001] as the most favorable growth direction when synthesized via chemical vapor deposition (350 Å diameter).^{24, 64} Zinc oxide surface (slab) calculations have revealed that the non-polar (10-10) surface undergoes a relaxation, self-healing the surface states in the band gap through a transfer of charge from zinc to oxygen.⁶⁵ Zinc oxide NWs grown along the [0001] have been shown to present the (10-10) surface.⁶⁶ The need to

preserve the symmetry of the wire's cross section and maintain the (10-10) surface determines the center of the wire (see Fig. 24). To maintain symmetry the axis of the 8 Å diameter NW intersects with atoms while the axis of the other two wires is centered in a hexagonal channel through the crystal lattice.

Unlike silicon, the need for a surface termination scheme is not critical if the non-polar surface is preserved on the surface of the ZnO NWs. The relaxation results in the tilting of the surface bond between anions (oxygen) and cations (zinc), parallel to the wire's axis. The oxygen atom is seen to move away from the axis while the zinc moves toward the center. Experimental results characterize this displacement by an angle of 10.1° (see Fig. 25).³⁹ The present calculation found it to be 9.6° in agreement with what is reported by Xiao Shen *et al.* using ultra-soft PBE.⁵⁶ Relaxation also results in the reduction of the bond length between the oxygen and zinc of the surface dimer pairs from 2.07 to 1.9 Å. A similar bond length contraction of 2.005 to 1.978 Å was calculated by Wang *et al.*⁶⁷ It is believed that this surface relaxation self-heals the in-gap surface states by transferring charge from the Zn to the O atoms.⁵⁵

Unlike the silicon NWs, the zinc oxide NWs will undergo a structural optimization. A series of data points was determined by creating multiple structure files, each with a different lattice parameter c . Those structures are then allowed to fully relax and each relaxed structure has an energy with a corresponding lattice vector c , $E_i(c_i)$.

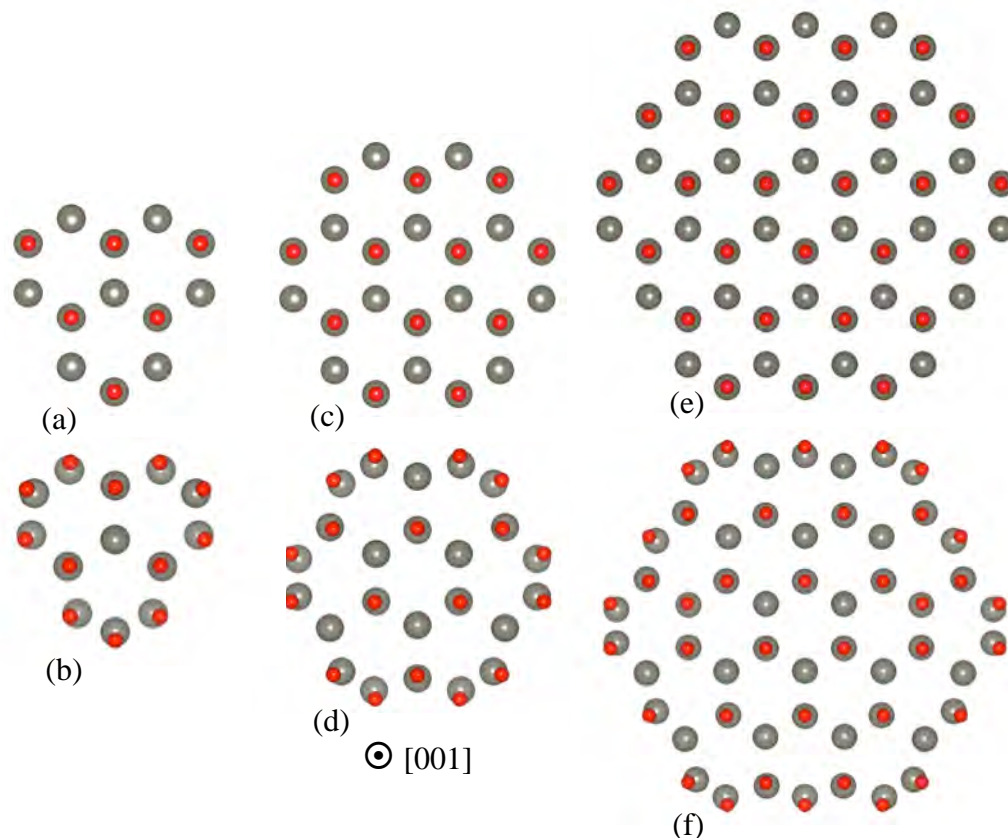


Figure 24. ZnO Nanowire Cross-Sections; looking onto the (001). (a) and (b) represent the ideal and relaxed nanowire of radius of 4 Å. (c) and (d) represent the ideal and relaxed structures of a wire with a radius of 5 Å. (e) and (f) represent the ideal and relaxed structures of a wire with a radius of 8.5 Å. For all relaxations a conjugate-gradient algorithm is used within a PAW PBE pseudopotential framework. The k-point mesh was chosen to be gamma centered, 4x4x24. Red is oxygen and grey is zinc. The non-polar (10-10) surface was preserved to reduce in gap states without H-passivation. The buckling of the surface can be seen in (b), (d), and (f).

The simulation cell of the NWs has a vacuum of 3.5 Å around the wire (7 Å between neighboring NWs). A 2nd order polynomial is used to fit the data points $E_i(c_i)$. This function is then minimized to determine the predicted ground-state energy configuration. Through what appears to be conservation of volume, if the lattice parameter c is lengthened then the radius of the relaxed NW is reduced, as reported in other theoretical investigations (DFT with PBE) into zinc oxide NWs.^{55, 67}

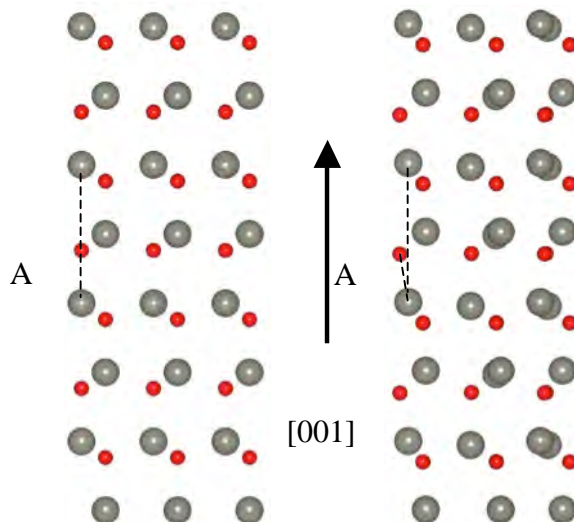


Figure 25. ZnO Nanowire Profile; (a) and (b) are the ideal and relaxed structures, respectively, for the 8 Å diameter nanowire. The relaxation causes a buckling of the surface bonds parallel to the z-axis. The bond direction between the surface Zn and O atoms is parallel to the wire's axis for the ideal case. For the relaxed structure the O atoms move out with respect to the Zn atoms. The buckling caused by relaxation is characterized by the bond angle at position "A" increasing from 0° to about 9.6° which is close to the theoretical value of 10.1° reported elsewhere. Similar surface buckling was seen on the other wires.

A gamma-centered mesh of 4x4x24 is used to sample k-space. This results in 150, 117, and 117 irreducible k-points for the 8, 10, and 17 Å diameter NWs, respectively. The ground-state lattice parameters for the zinc oxide NWs correspond to the lattice parameters $c=5.41997$, $c=5.4163$, and $c=5.3701$ Å for the 8, 10, and 17 Å diameter NWs respectively. The electronic structure were determined with the calculated lattice parameter values mention above. Both the total density-of-states and the band structure can be seen in Figures 26 to 28.

The band gap for the 8 Å diameter wire is calculated to be 1.59 eV. That is a factor of 2.2 larger than the calculated band gap of Bulk ZnO. Other DFT calculations on the same 8 Å diameter NW have reported band gap values of 1.64⁵⁶, 1.888⁶⁷ and 1.7⁶⁸ eV. As seen in Figure 26, the density-of-states for the 8 Å diameter NW has a sharp peak in the energy range of -0.3 and 0.0 eV. As suggested by Dr. Dresselhaus this

characteristic sharp peak could indicate a high electrical conductivity and Seebeck coefficient and therefore a potentially high ZT. The smallest wire calculated here, 8 Å diameter, had the largest peak in its DOS along the edges of the band gap. This sharp peak can be attributed to the effects of quantum confinement. The calculation of the thermoelectric figure-of-merit reveals that the 8 Å NW also has the highest ZT. This supports the idea proposed by Dr. Dresselhaus, that a sharp peak in the DOS along the band edges could indicate a high ZT (see Fig. 29).¹

Two prominent effects can be noticed when increasing the diameter of a ZnO NW from 8 to 10 Å; 1) The band gap is reduced from 1.59 to 1.369 eV (see Fig. 26 & 27) and 2) The sharp peak seen in the DOS of the 8 Å NW is reduced. Increasing the diameter reduces the effects of quantum confinement. Overlaying the band structures of both the 8 and 10 Å reveals that the band dispersion is not significantly altered by the increase in diameter. The calculated band gap of the 10 Å NW is found to be 1.875 times larger than the calculated band gap of Bulk ZnO.

If the diameter is further increased from 10 to 17 Å the calculated band gap becomes 1.111 eV, 41% larger than the calculated band gap of bulk ZnO. The characteristic sharp peak seen in the DOS of the 8 Å diameter wire almost completely disappear in the 17 Å diameter wire. For a closer picture of the sharp peaks in DOS at the lowest conduction bands please refer to Figure 30. The thermoelectric calculations reveal that the 17 Å diameter NW has the lowest ZT of all three wires. The relationship between the diameter of NWs and the band gap found here, supports the work of others.⁶⁷⁻⁶⁹ The values for the band gaps reported in references 70-72 are not comparable

because different calculation methodology was employed, but the overall trends found here correlate very well with those reported.

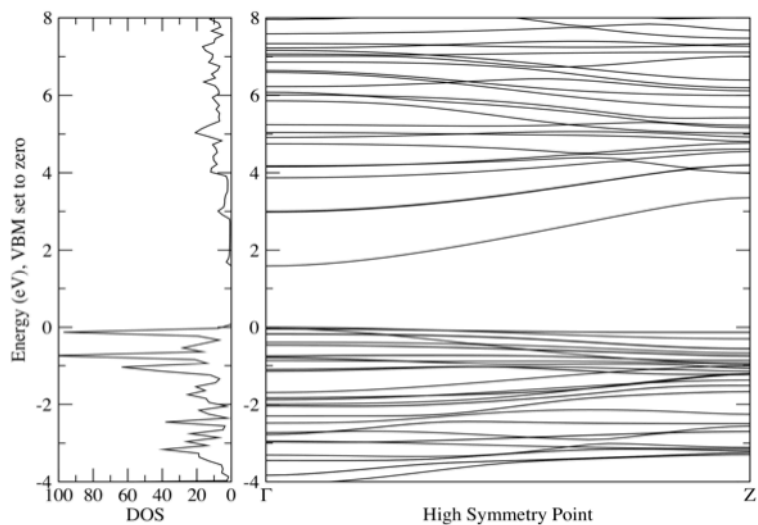


Figure 26. Electronic Structure of the ZnO NW with 8 Å Diameter. Ground-state lattice parameter $c = 5.41997$ Å. A calculated band gap of 1.59 eV was found, factor of 2.2 higher than the calculated bulk value. The effects of quantum confinement can be seen in the sharp peak at the highest valence bands in the DOS (electrons/unit cell), when compared to Bulk ZnO.

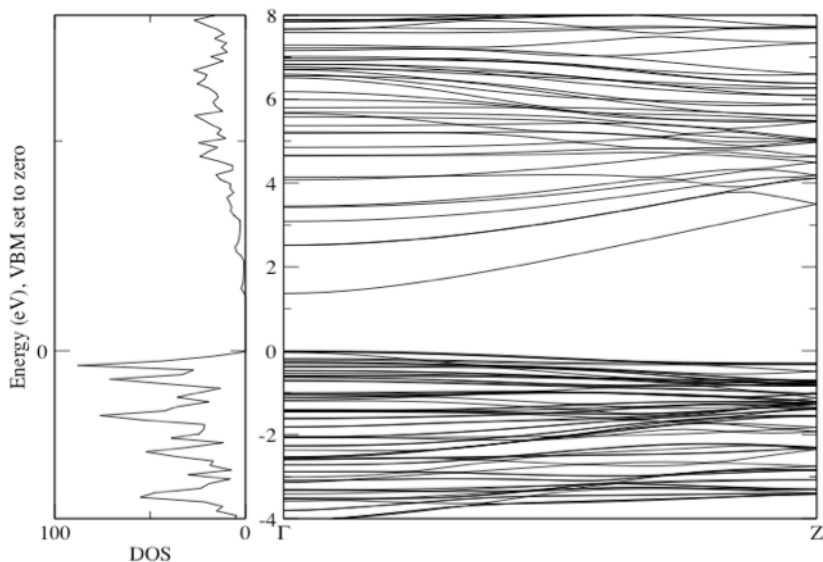


Figure 27. Electronic Structure of the ZnO NW with a 10 Å Diameter. Ground-state lattice parameter $c = 5.41637$ Å. A band gap of 1.369 eV was found. A factor of 1.875 larger than the calculated bulk value, 0.73 eV. The effects of quantum confinement can be seen in sharp peak in the DOS (electrons/unit cell) at the highest valence bands, when compared to bulk.

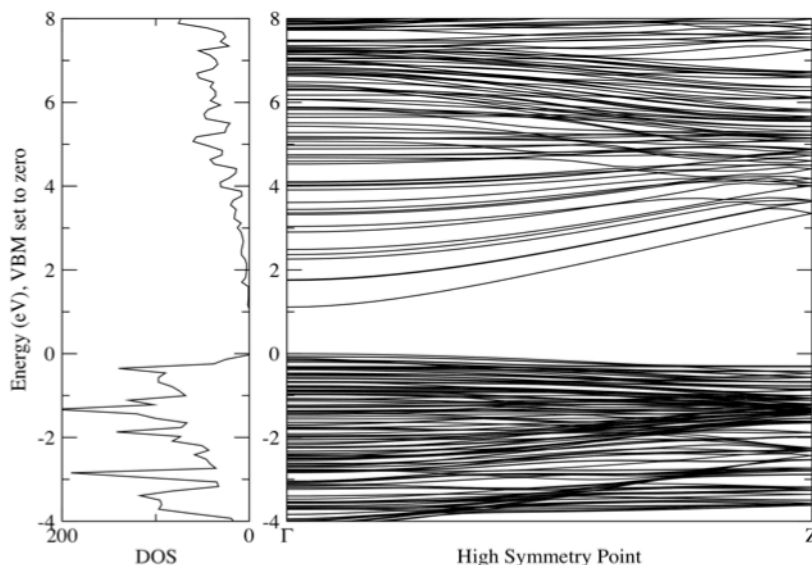


Figure 28. Electronic Structure of the ZnO NW with a 17 Å Diameter. Ground-state lattice parameter $c = 5.37013$ Å. A band gap of 1.111 eV was found. A factor of 1.52 higher than the calculated bulk value, 0.73 eV. The effects of quantum confinement are not as dramatic as the smaller wires. DOS in unit of number of electrons/simulation cell.

The thermoelectric properties are calculated for the ZnO NWs at 300 K. The relaxation time used to calculate the electrical conductivity and the electronic component of thermal conductivity of the ZnO NWs is 30×10^{-15} seconds. The thermoelectric properties of the NWs were calculated with the same settings used for bulk. Please refer back to the thermoelectric properties of bulk ZnO for more details

The lattice component of thermal conductivity κ_l used for bulk at 300 K is 23 W/Km. This value was taken from experimental data reported by Ohtaki *et al.*^{9, 10}. Through the molecular dynamics calculations of Galli *et al.* Si NWs were shown to reduce the lattice component of thermal conductivity from bulk by two orders of magnitude (from 100 to 2 W/Km).²⁷ Literature research found one molecular dynamics calculation on ZnO NWs oriented in the [0110] direction with diameters ranging from 18.95 to 40.81 Å. It reports a lattice component of thermal conductivity of 8.3-8.6 W/Km

at 500 K for the range of NW diameters. An overall reduction in κ_l of one order of magnitude over bulk is reported.⁷⁰ In the present work the bulk value of 23 W/Km is used to calculate ZT for the NWs as well. This will result in the lowest possible value for the ZT of the NWs.

The carrier concentration dependent thermoelectric properties of ZnO NWs can be seen in Figure 29. In the figure the black, red, and blue lines represent the 8, 10, and 17 Å ZnO NWs respectively. The 10 and 17 Å ZnO NWs have similar electrical conductivity with values of $650 (\Omega\text{cm})^{-1}$ at 10^{20} cm^{-3} . The electrical conductivity of the 8 Å NW was found to be $330 (\Omega\text{cm})^{-1}$ at 10^{20} cm^{-3} . This is a reduction of one order of magnitude from the calculated electrical conductivity of bulk ZnO, $\sigma_{\text{bulk}}=3250 (\Omega\text{cm})^{-1}$.

The electronic component of thermal conductivity at a carrier concentration of 10^{19} cm^{-3} is found to be 0.197, 0.25, and 0.21 W/Km for the 8, 10, and 17 Å ZnO NWs, respectively. These are all reductions from the 0.42 W/Km calculated for bulk ZnO at the same carrier concentration. Therefore the use of NWs has been seen to reduce the lattice component of thermal conductivity from bulk for both silicon and ZnO. However, the reduction is less significant for ZnO NWs compared to silicon NWs.

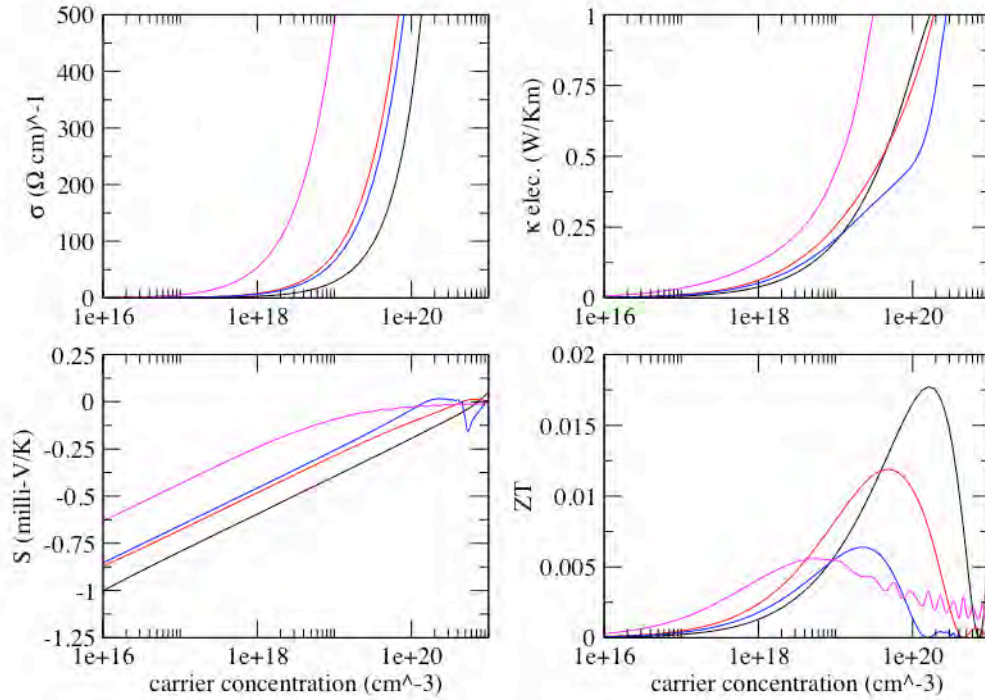


Figure 29. Thermoelectric Properties of ZnO NWs at 300 K. (a) electrical conductivity σ , (b) electronic contribution to thermal conductivity κ_e , (c) Seebeck coefficient S , (d) Figure-of-merit ZT . The 0.8 nm, 1 nm and the 1.7 nm NWs are represented by the black, red, and blue respectively. The magenta line represents the bulk at 300 K with a $\kappa_l=23$ W/Km. The NW's ZT is calculated with $\kappa_l=23$ W/Km represented by the black, red, and blue lines. The relaxation time used was 30×10^{-15} , determined by the MD calculations of Baxter *et al.*

It was found that the 8 Å diameter NW has the lowest Seebeck coefficient with a value of -0.4 mV/K at 10^{19} cm⁻³. The highest Seebeck coefficient between the three NWs was calculated for the 17 Å diameter NW, -0.27 mV/K at the same carrier concentration. The Seebeck coefficient of the 10 Å diameter wire fell in-between, -0.3 mV/K at 10^{19} cm⁻³.

The thermoelectric figure-of-merit was highest for the 8 Å diameter wire with a value of 0.0175 optimized at a carrier concentration of 1.73×10^{20} cm⁻³. This is a factor of 3.14 larger than the ZT calculated for bulk ZnO at 300 K. The 10 Å diameter wire was found to have a $ZT=0.012$ optimized at a carrier concentration of 5.03×10^{19} cm⁻³. The 17 Å diameter wire was found to have a $ZT=0.006$ at a carrier concentration of 2.3×10^{19}

cm^{-3} . It can be seen that as the wire diameter increases to 17 Å ZT approaches the bulk value at 300 K.

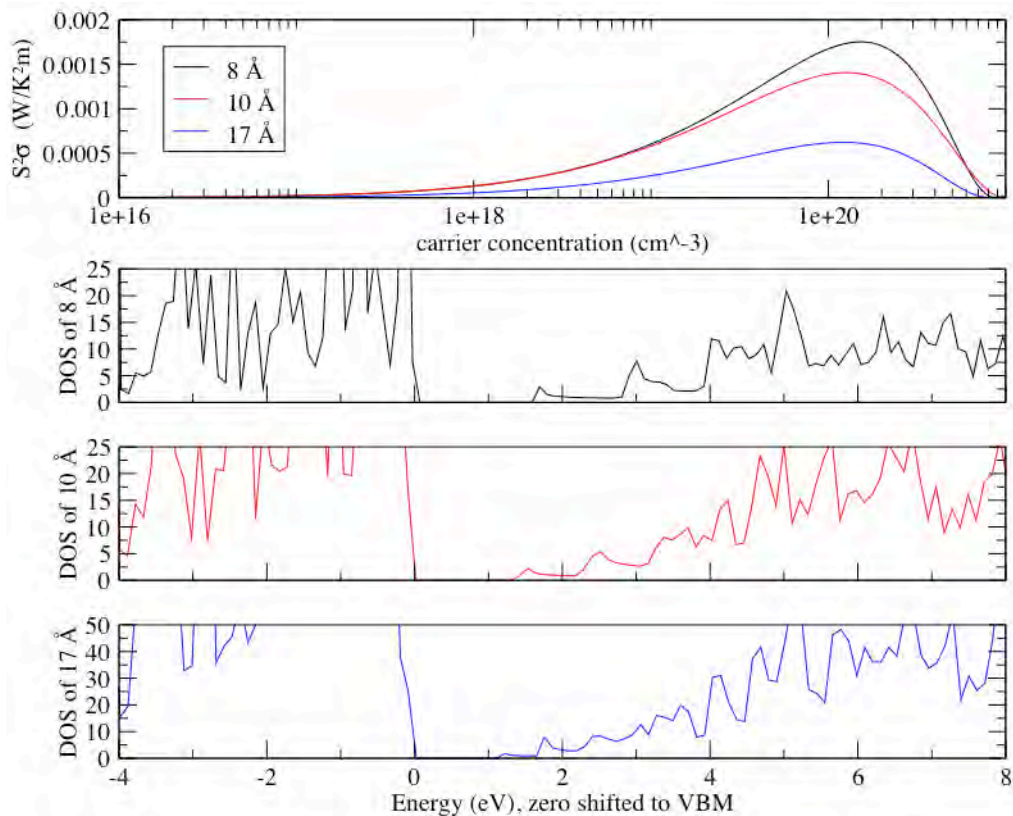


Figure 30. Thermopower of ZnO NWs at 300 K. (a) Thermopower of 8, 10, and 17 Å NWs (b) DOS of 8 Å NW, (c) DOS of 10 Å NW, (d) DOS of 17 Å NW.

Figure 30 reveals the relationship between the thermopower and the sharp peaks of the lowest conduction bands in the density of states (1-2 eV). The 8 Å diameter wire has the steepest DOS at the lowest conduction bands and also the highest calculated thermopower of 0.0017 $\text{W/K}^2\text{m}$. The 17 Å diameter wire has the least steep DOS at the lowest conduction bands and the lowest thermopower, 0.0005 $\text{W/K}^2\text{m}$. The 10 Å diameter wire fell in-between with a value of 0.0015 $\text{W/K}^2\text{m}$.

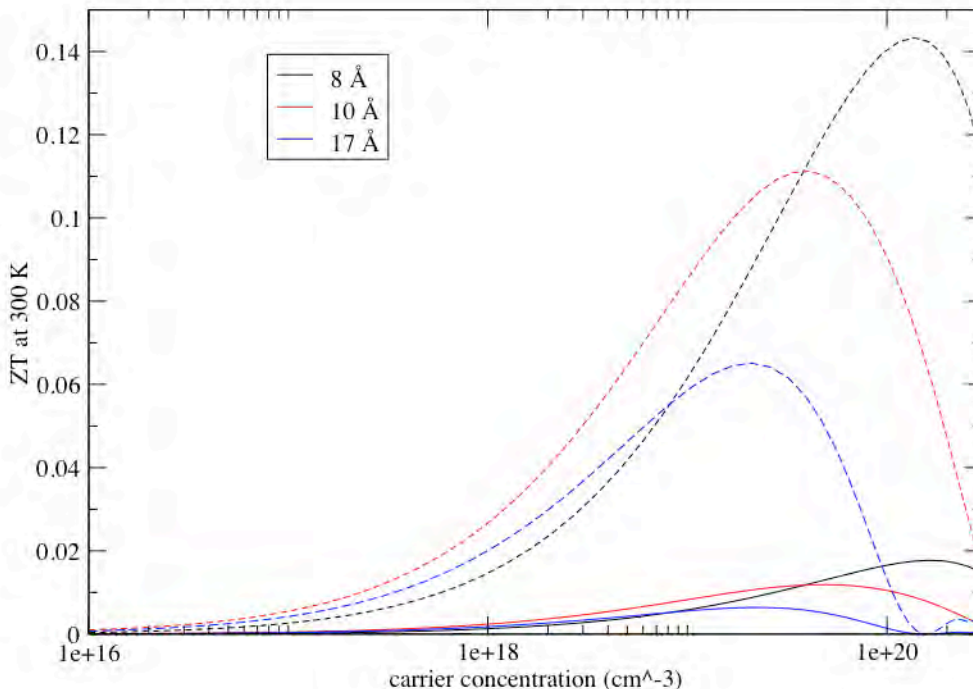


Figure 31. ZT of ZnO Nanowires; The 8, 10, and 17, Å diameter NWs are represented by black, red, and blue lines respectively. The solid lines are calculated using the bulk value of κ_l , 23 W/Km. The dashed lines are calculated with a κ_l assuming a decrease by one order of magnitude, 2.3 W/Km.

The silicon NW oriented in the [0001] direction had the highest thermopower of 0.62 mW/K²m. The thermopower for the 8 Å ZnO NW was found to be 2.74 times larger than that of best silicon NW, yet the calculated ZT of the ZnO NWs was found to be lower than that of silicon NWs. This is because the ZTs in Figure 29 represent the lowest possible values and do not account for the reduction in κ_l through lowering the dimensions. Molecular dynamics calculations on ZnO NWs have reported a ten fold decrease in κ_l from bulk for wires oriented in the [01-10] direction with diameters in range of 18.95 Å to 40.81 Å.⁷⁰ If a similar decrease can be assumed for ZnO NWs of other orientations then the κ_l for the ZnO oriented in the [0001] may hypothetically be as low as 2.3 W/Km. This assumption increases the calculated ZTs by a factor of 8 from the

value calculated using bulk κ_l (as seen in Fig. 32). ZT is the highest for the 8 Å diameter wire with a value of 0.14, 28 times larger than the ZT calculated for bulk ZnO. Therefore the dotted lines represent the hypothetical maximum for the ZT of ZnO NWs at 300 K.

CHAPTER 5

CONCLUDING REMARKS

Density functional theory was used in conjunction with Boltzmann transport theory to examine the thermoelectric properties of semiconductor nanowires. The thermoelectric properties dependence on growth direction was explored in the calculations related to silicon, and the ZnO calculations investigated the dependence on the nanowire's diameter. It was found that both silicon and ZnO nanowires demonstrate an improvement in thermoelectric efficiency over bulk. However the increase is not significant enough to make silicon or ZnO nanowire systems viable alternatives to present technologies. The electronic component of thermal conductivity of both silicon and ZnO are found to be reduced by at least half of the bulk value, but unfortunately electrical conductivity was also considerably reduced.

The silicon nanowire oriented in the [001] direction was found to have the largest $ZT_{[001]}=0.08$. This is an increase of a factor of ~ 11 over the calculated $ZT_{Si\ bulk}=0.007$, but two orders of magnitude smaller than the value of 2.5 reported by Galli *et al.*²⁷ The large discrepancy between what was reported by Galli *et al.* and the value may be attributed to the choice of surface termination and relaxation time. The values calculated for silicon nanowires reported here were independently verified by Dr. Denis Demchenko and Dr. Byounghak Lee.

The ZnO nanowires were found to have increased thermal efficiency when compared to bulk ZnO. On the low side an increase of a factor of 3.14 was noticed over bulk ZnO. This minimum ZT was calculated with the lattice component of thermal conductivity of bulk ZnO. The maximum ZT was calculated with a hypothetical lattice component of thermal conductivity one order of magnitude less than the lattice component of thermal conductivity. This results in an increase of ZT by a factor of 28 over bulk ZT values (see Fig. 32). Because the ZnO NWs have a higher thermopower than the silicon NWs they have the potential to have a higher ZT. Further molecular dynamics calculations could remove the ambiguity from the lattice component of thermal conductivity.

REFERENCES

1. M. S. Dresselhaus, G. Chen, M. Y. Tang, R. Yang, H. Lee, D. Wang, Z. Ren, J.-P. Fleurial and P. Gogna, *Advanced Materials* **19**, 1-12 (2007).
2. D. M. Rowe, in *Thermoelectrics handbook: macro to nano*, edited by D. M. Rowe (Taylor and Francis, Boca Raton, 2006), pp. 1-1 thru 1-9.
3. G. J. Snyder and E. S. Toberer, *Nature Materials* **7**, 105-114 (2008).
4. L. D. Hicks, T. C. Harman, X. Sun and M. S. Dresselhaus, *Physical Review B* **53** (16), R10493-R10496 (1996).
5. L. D. Hicks and M. S. Dresselhaus, *Physical Review B* **47**, 12727 (1997).
6. L. D. Hicks and M. S. Dresselhaus, *Physical Review B* **47** (19), 12727-12731 (1993).
7. D. Emin, in *Thermoelectrics handbook: macro to nano*, edited by D. M. Rowe (Taylor and Francis, Boca Raton, 2006), pp. 5-2.
8. D. Emin, in *Thermoelectric handbook: macro to nano*, edited by D. M. Rowe (Taylor and Francis, Boca Raton, 2006), pp. 5-3 thru 5-5.
9. M. Ohtaki, T. Tsubota, K. Eguchi and H. Arai, *Journal of Applied Physics* **79** (3), 1816-1818 (1995).
10. T. Tsubota, M. Ohtaki, K. Eguchi and H. Arai, *Journal of Material Chemistry* **7** (1), 85-90 (1997).
11. N. W. Ashcroft and N. D. Mermin, *Solid State Physics*. (Thomson Learning, 1976).
12. J. I. Gersten and F. W. Smith, *The Physics and Chemistry of Materials*. (John Wiley & Sons, Inc., New York, 2001).
13. T. K. Reynolds, J. G. Bales, R. F. Kelley and F. J. DiSalvo, in *Chemistry, Physics, and Materials Science of Thermoelectric Materials: Beyond Bismuth Telluride*, edited by M. G. Kanatzidis, S. D. Mahanti and T. P. Hogan (Kluwer Academics / Plenum Publishers, New York, 2003).

14. M. S. Dresselhaus, Y.-M. Lin, O. Rabin, M. R. Black, S. B. Cronin and G. Dresselhaus, in *Chemistry, Physics, and Material Science of Thermoelectric Materials: Beyond Bismuth Telluride*, edited by M. G. Kanatzidis, S. D. Mahanti and T. P. Hogan (Kluwe Academics / Plenum Publishers, New York, 2003).
15. L. D. Hicks, *Physical Review B* **47**, 16631 (1997).
16. A. I. Boukai, Y. Bunimovich, M. Tahir-Kheli, J.-K. Yu, W. A. G. III and J. R. Heath, *Nature* **451**, 168-171 (2008).
17. D. I. Bilc, *Electronic and Transport Properties of Novel Thermoelectrics*. (VDM Verlag Dr. Muller Aktiengesellschaft & Co. KG, 2009).
18. J. P. Heremans, C. M. Thrush, Z. B. Zhang, X. Z. Sun, M. S. Dresselhaus, J. Y. Ying and D. T. Morelli, *Physical Review B* **58**, R10091-10095 (1998).
19. Y.-M. Lin, S. B. Cronin, J. Y. Ying, M. S. Dresselhaus and J. P. Heremans, *Applied Physics Letters* **79**, 3944-3946 (2000).
20. O. Rabin, Y.-M. Lin and M. S. Dresselhaus, *Applied Physics Letters* **79**, 81-83 (2001).
21. Y.-M. Lin, O. Rabin, S. B. Cronin, J. Y. Ying and M. S. Dresselhaus, *Applied Physics Letters* **80**, 2493-2495 (2002).
22. Y.-M. Lin, S. B. Cronin, O. Rabin, J. Y. Ying and M. S. Dresselhaus, *Applied Physics Letters* **79**, 677-679 (2001).
23. Y. Zhang, Y. Tang, N. Wang, C. Lee, I. Bello and S. Lee, *Journal of Crystal Growth* **197**, 136 (1999).
24. W. Q. Yang, H. B. Huo, L. Dai, R. M. Ma, S. F. Liu, G. Z. Ran, B. Shen, C. L. Lin and G. G. Qin, *Nanotechnology* **17**, 4868-4872 (2006).
25. J.-h. Lee, G. Galli and J. Grossman, *Nano Letters* **8** (2008).
26. L. Weber and E. Gmelin, *Applied Physics A* **53**, 136-140 (1991).
27. G. Galli, *Nano Letters* **8** (4), 1111 (2008).
28. S. Sharama, T. Kamin and R. Williams, *Applied Physics A* **80**, 1225 (2005).
29. M. Saifislam, S. Sharama, T. Kamis and R. Williams, *Applied Physics A* **80**, 1133 (2005).
30. X. Yang and e. al., *Journal of Crystal Growth* **257**, 69 (2003).
31. T. Vo, A. J. Williamson and G. Galli, *Physical Review B* **74**, 045116 (2006).

32. A. Saita, F. Buda, G. Fiumara and P. Giaquinta, *Physical Review B* **53**, 1446 (1996).
33. X. Zhao, C. Wei, L. Wang and M. Chou, *Physical Review Letters* **92**, 236805 (2004).
34. A. Hochbaum, R. Chen, R. D. Delgado, E. Garnett, A. Majumdar and P. Yang, *Nature* **45**, 163 (2007).
35. N. Mingo, L. Yang, D. Li and A. Majumdar, *Nano Letters* **3** (1713) (2003).
36. G. Kresse and J. Furthmuller, *Computer Material Science* **6** (1), 15-50 (1996).
37. G. Kresse and J. Furthmuller, *Physical Review B* **54** (16), 11169-11186 (1996).
38. G. Kresse and D. Joubert, *Physical Review B* **59** (3), 1758-1775 (1999).
39. G. K. H. Madsen and D. J. Singh, *Computer Physics Communications* **175**, 67-71 (2006).
40. R. L. Liboff, *Introductory Quantum Mechanics*, 4th ed. (Addison Wesley, San Francisco, 2003).
41. K. Capelle, *Brazilian Journal of Physics* **36** (4A), 1318-1343 (2006).
42. P. Hohenberg and W. Kohn, *Physical Review* **136**, B864 (1964).
43. W. Kohn and L. J. Sham, *Physical Review* **146**, A1133 (1965).
44. J. P. Perdew, K. Burke and M. Ernzerhof, *Physical Review Letters* **77**, 3865-3868 (1996).
45. N. P. Blake and M. Metiu, in *Chemistry, Physics, and Materials Science of Thermoelectric Materials: Beyond Bismuth Telluride*, edited by M. G. Kanatzidis (Kluwer Academics/Plenum Publishers, 2003).
46. C. M. Hurd, *The Hall Effect in Metals and Alloys*. (Plenum Press, New York, 1972).
47. P. E. Blochl, *Physical Review B* **50** (24), 17953-17979 (1994).
48. A. Gaymann, *Physical Review B* **52** (23), 16486 (1995).
49. N. Mingo, *Physical Review B* **68**, 113308 (2003).
50. D. R. Lide, *CRC Handbook of Chemistry and Physics*, 74th ed. (CRC Press, Boca Raton, 1993).

51. D. R. Lide, *CRC Handbook of Chemistry and Physics*. (CRC Press, Boca Raton, 1997).
52. Ü. Özgür, *Journal of Applied Physics* **98**, 041301 (2005).
53. H. Schulz and K. H. Theimann, *Solid State Communications* **32**, 783 (1979).
54. U. Rössler and Ed., in *Landolt-Bornstein, New Series, Group III* (1999), Vol. 41B.
55. G. Cicero, A. Ferretti and A. Catellani, *Physical Review B* **80**, 201304 (2009).
56. X. Shen, M. R. Pederson, J.-C. Zheng, J. W. Davenport, J. T. Muckerman and P. B. Allen, (Brookhaven National Laboratory, 2009).
57. X. Pengshou, S. Yuming, S. Chaoshu, Z. Faqiang and P. Haibin, *Science in China* **44** (9), 1174-1181 (2001).
58. P. Schröer, P. Krüger and J. Pollman, *Physical Review B* **47**, 6971 (1993).
59. P. Schröer, P. Krüger and J. Pullman, *Physical Review B* **48**, 18264 (1993).
60. S. B. Zhang, S. H. Wei and A. Zunger, *Physical Review B* **52**, 13975 (1995).
61. S. H. Wei and A. Zunger, *Physical Review B* **37**, 8958 (1988).
62. J. B. Baxter and C. A. Schmuttenmair, *Journal of Physical Chemistry B* **110**, 25229-25239 (2006).
63. Ü. Özgür, *Journal of Applied Physics* **98**, 041301 (2005).
64. P. C. Chang, Z. Fan, C.-J. Chien, D. Stichtenoth, C. Ronning and J. G. Lu, *Applied Physics Letters* **89**, 133113 (2006).
65. N. L. Marana, V. M. Longo, E. Longo, J. B. L. Martins and J. R. Sambrano, *Journal of Physical Chemistry A* **112**, 8958-8963 (2008).
66. M. Law, L. E. Green, J. C. Johnson, R. Saykally and P. Yang, *Nature Materials* **4**, 455 (2005).
67. B. Wang, J. Zhao, J. Jia, D. Shi, J. Wan and G. Wang, *Applied Physics Letters* **93**, 021918 (2008).
68. Z. Fu-Chun, Z. Zhi-Yong, Z. Wei-Hu, Y. Jun-Feng and Y. Jiang-Ni, *Chinese Physics B* **18** (6), 2508-2513 (2009).
69. J. Li and L.-W. Wang, *Physical Review B* **72**, 125325 (2005).
70. A. J. Kulkarni and M. Zhou, *Nanotechnology* **18**, 435706 (2007).

